Cell migration through 3D confining pores: speed accelerations by deformation and recoil of the nucleus

Article (Accepted Version)

Cell migration through 3D confining pores: speed accelerations by deformation and recoil of the nucleus

Marina Krause [a1], Feng Wei Yang [b1], Mariska te Lindert [a], Philipp Isermann [c], Jan Schepens [a†], Ralph JA Maas [a], Khouloud Eid [a], Chandrasekhar Venkataraman [b], Jan Lammerding [c], Anotida Madzvamuse [b], Wiljan Hendriks [a], Joost te Riet [d], Katarina Wolf [a]

[1] MK and FWY contributed equally to this work.

[a] Department of Cell Biology, Radboud University Medical Center, 6525 GA Nijmegen, the Netherlands

[b] Department of Mathematics, School of Mathematical and Physical Sciences, University of Sussex, BN1 9QH, Falmer, Brighton, United Kingdom

[c] Weill Institute for Cell and Molecular Biology, Meinig School of Biomedical Engineering Cornell University, Ithaca, NY 14853; USA

[d] Department of Tumor Immunology, Radboud University Medical Center, 6525 GA Nijmegen, the Netherlands

[†] Deceased

Corresponding author:

Dr. Katarina Wolf
Dept. of Cell Biology, Radboud Institute for Molecular Life Sciences (RIMLS)
Geert Grooteplein Zuid 26-28
6525 GA Nijmegen
Tel: +31 24 361 4296
E-mail: katarina.wolf@radboudumc.nl

Short title: Nuclear oscillation in cell migration

Key words: Tumor cell, migration in confinement, speed oscillation, nuclear shape change, cell cycle, chromatin condensation

Abstract

Directional cell migration in dense three-dimensional (3D) environments critically depends upon shape adaptation and is impeded depending on the size and rigidity of the nucleus. Accordingly, the nucleus is primarily understood as a physical obstacle, however, its pro-migratory functions by step-wise deformation and reshaping remain unclear. Using atomic force spectroscopy, time-lapse fluorescence microscopy and shape change analysis tools, we determined nuclear size, deformability, morphology and shape change of HT1080 fibrosarcoma cells expressing the Fucci cell cycle indicator or being pre-treated with chromatin-decondensating agent TSA. We show oscillating peak accelerations during migration through 3D collagen matrices and microdevices that occur during shape reversion of deformed nuclei (recoil), and increase with confinement. During G1 cell cycle phase, nucleus stiffness was increased and yielded further increased speed fluctuations together with sustained cell migration rates in confinement as compared to interphase populations, or to periods of intrinsic nuclear softening in the S/G2 cell cycle phase. Likewise, nuclear softening by pharmacological chromatin decondensation or after lamin A/C depletion reduced peak oscillations in confinement. In conclusion, deformation and recoil of the stiff nucleus contributes to saltatory locomotion in dense tissues.

Introduction

Cell migration is an essential process during development, tissue maintenance and immune function, but is also of importance during pathological cell invasion, including cancer metastasis [1]. Whenever cells move through connective tissue which consists of spatially and mechanically complex 3D protein meshworks [2], they respond to mechanical confinement by changing shape. In vivo, migrating cells encounter physical challenges composed of microstructural extracellular matrix (ECM) networks and tissue tracks with 1-30 μm in width which are comparable to or smaller than the cell diameter of migrating cells ranging from 8 to 15 μm [3,4]. The nucleus is the largest and stiffest cell organelle that reaches 2-10 fold higher stiffness values than the surrounding cytoplasm [5,6] and plays a pivotal role in cell deformation. Accordingly, under ECM space conditions matching the nuclear diameter, or by cell-derived proteolytic tissue degradation to create a low resistance path that matches the thickest cell diameter, cell migration is not impeded [4]. In contrast, in confining ECM environments, the nucleus will deform and adapt to the constraints of the ECM, but at the same time also form a mechanical obstacle which will gradually slow down migration [4,7-9].

The nucleus is both positioned and transported by the coordinated functions of microtubules, leading edge protrusion, integrin attachment to the surrounding substrate, contractile actin cytoskeleton fibers and the linker of cytoskeleton and nucleoskeleton (LINC) complex physically linking the chromatin to the cytoskeleton. This leads to alternating force build-up at the front, and contraction of the rear concomitant with rear end integrin de-attachment from ECM, which will move the nucleus forward. Thus, alternating cycles of mechanical pulling and pushing act upon the nucleus during cell migration [4,7,10-12]. Previously we have proposed a multi-step translocation cycle of the nucleus during 3D cell migration consisting of (I) pressure application by the external constraint onto the nuclear membrane in the direction of migration, (II) beginning deformation of the nucleus by the formation of a local prolapse slowing down migration, (III) gliding of the compressed and deformed nucleus through the pore, and (IV) rear release connected to rapid forward pushing and rounding (recoil) of the nucleus [13]. Implicit to this cyclic process, the migration delay during phase II is consistent with the ‘physical barrier’ function of the nucleus and might represent a phase of storage of deformation energy, which is released as propulsive energy during phase IV, leading to short phases of increased migration. It is, however, not clear whether and to what extent and by which physical characteristics the nucleus contributes to acceleration of cell migration.

The overall stiffness, or elasticity, of the nucleus in an intact cell is dependent on a

number of structural determinants, including A-type lamins that are part of the nuclear lamin network underlying the double nuclear membranes, as well as the organization of chromatin [14-20]. The chromatin packing state is variable and changes according to the transcriptional needs, the extent of DNA repair, and the cell cycle phase, particularly when the diploidic G1 stage undergoes DNA replication in S-phase to reach the tetraploidic G2 phase stage. Each of these events involve changes in DNA organization, with transient and reversible conversions of dense heterochromatin to more open euchromatin by histone acetylation or de-methylation [21,22]. These two latter processes lead to chromatin decondensation and thus nuclear softening (deformability) and concomitant size increase [23-27]. Conversely, chromatin condensation increases nuclear compaction and stiffness in conjunction with smaller size, as well as migration in wound healing and transwell chamber assays [20]. However, how these complex physical alterations of the nuclear interior impact shape change and migration in 3D confining environments remains to be assessed. In addition, it is unclear how softening of the nucleus i.e., by lamin A/C reduction [28-30], affects nuclear recoil when cells exit confined space.

Here, we used independent strategies of altered nuclear elasticity by chromatin condensation state and lamin A/C expression, and probed how these affect nuclear deformation and reshaping, as well as related migration patterns and rates. By comparing chromatin-compacted G1 cell cycle phase cells to cells migrating during interphase or S/G2 phase, or by treating cells with the chromatin decondensating compound Trichostatin A (TSA), we co-registered speed oscillations and nuclear deformations. In addition, we developed a computational approach to calculate fluctuations of nuclear shapes during each migration phase. Our results indicate that deformation of the elastic nucleus during passage of a constriction generates a recoil event that transforms into nuclear reshaping by rounding and, simultaneously, boosts nuclear propulsion and instantaneous migration velocity.

Results

Stiff G1 cell cycle phase cells maintain fast migration in confinement associated with shape change. To investigate the effect of the cell cycle on 3D migration, we generated HT1080 cells stably expressing Fucci, a fluorescent ubiquitination-based cell cycle indicator [31,32] (Fig. S1A). The expression of Cdt1-Kusabira-Orange2 in G1 cells and Geminin-Azami-Green1 in S/G2/M cells enabled us to visualize the forward progression of the cell cycle as G1, S-Start, and S/G2 phase by detecting either only red, overlapping red and green, or only green signal (Figs. 1A;

S2A; Movie S1). From all cells of a subconfluent 2D culture that expressed fluorescence, on average 28% of the cells were in G1, 14% in G1-to-S transition, and 58% in S/G2 phase, detected microscopically or by flow cytometry (Fig. S1B). In accordance with earlier findings [26,32,33], the nuclear area of cells during cycle progression from G1 to S/G2 phase increased by 23% (in cell culture) or 53% (after embedding in 3D collagen matrices), respectively (Fig. S1C; S2B).

To confirm that the rigidity of the nucleus decreases with cell cycle progression in HT1080 cells, we probed cultured Fucci sensor expressing cells by atomic force spectroscopy (AFS), using a bead-coupled cantilever (Fig. S1D). With transition from G1 to S/G2 phase, cell deformation increased by 1.4-fold (Fig. 1B) and, consequently, the calculated elastic moduli in G1 cells (991 ± 415 Pa) decreased by 23% after transit to S/G2 phase (767 ± 455 Pa), in line with previous data using HeLa cells [26]. Accordingly, due to increased chromatin condensation in G1 as compared to S/G2 cells, we calculated an 1.4 fold decrease in dissipation energy in G1 phase cells (Fig. S1D-G). Collectively, our findings confirmed that cells in G1 have stiffer and less viscous nuclei compared to cells in S/G2, consistent with a higher chromatin compaction status in the nucleus of G1 cells.

Next, the impact of cell cycle progression on HT1080 cell migration efficacy through collagen lattices of was tested. During polymerization of collagen into fibrillar networks, interfibrillar spaces of heterogenous size are formed. Pores that are smaller than the cross section of the polarized cell body will confine the migrating cell and its nucleus, whereas adjacent, more open spaces will provide sufficient space for a cell to move forward (Fig. 1C). Of note, many activated or cancer cell types including HT1080 fibrosarcoma cells, express a range of matrix metalloproteinases (MMPs) such as MMP-14, and migrate through collagen matrices of heterogenous pore area range (i.e. 5-25 μm^2) by proteolytic remodeling of collagen fibrils, creating paths with 50-100 μm^2 pore areas that match the respective cell cross sections [34]. In this setting, MMP broad spectrum inhibitor GM6001 inhibits collagen degradation and increases the deformation of cell and nucleus during migration by 2-3 fold, reaching cross sections of around 25 (10-40) μm^2 [4,35]. These deformation ranges matched with the capacity of HeLa G1 cell cycle cells to penetrate pores of around 10 and 40 μm^2 cross section, as shown in [26]. To test in context how cell deformation and migration speed are altered with transit from G1 to S/G2 phase, migrating HT1080-Fucci cells were optically separated into Fucci-red, -yellow and -green (Fig. 1D). Proteolytic migration speed of a G1 phase cell population in 3D collagen lattices was 0.4 μm/min and reduced by 18% in S/G2 phase cells, whereas at conditions of confinement,

migration in S/G2 cells was increasingly compromised by 42%, reaching 0.23 µm/min (Fig. 1E). A similar deceleration was confirmed during individual cell migration monitored during transition from G1 to S/G2 phase, yielding 50% decreased migration speed (Figs. S2C, two most upper graphs; Movie S1). The reduced migration rates of the S/G2 cell population may result from complex nuclear properties, including increased nuclear size and chromatin decondensation during S phase and prior to mitosis, combined with reduced cell adhesion and actomyosin-mediated stiffness [26]. We asked, however, how cells in G1 phase cells could maintain speed in confinement despite a comparably stiffer nucleus.

To gain insight into the extent of nuclear deformation relative to speed changes during migration in confinement, we thresholded nuclear shapes (Fig. 1F; Movies S1, right section; S2) and quantified respective shape change over time as nuclear irregularity index (NII; Fig. 1G) [36]. The NII determines the level of shape deviation of the nucleus from a circle, and was chosen over more widely-used nucleus roundness measurements because of its higher sensitivity (Fig. S3). Whereas nuclei in S/G2 phase were more roundish, nuclei in G1 phase adopted somewhat longer and more irregular shapes, which was increased by the presence of GM6001 (Fig. 1H). These irregular shape values changed stronger over consecutive time points and were, when MMPs were inhibited, increased by 2.4-fold in G1 phase but only 1.3-fold in S/G2 phase cells (Fig. 1I). To support these findings on dynamic nuclear shape changes, we included nuclear fluctuation analysis (Fig. 1J, left; Movie S3). This tool calculates the difference between consecutive nuclear shapes, thus the shape change. To exclude errors due to a directional change of a cell during migration, nuclear shapes were rotated for maximal overlap. Again, nuclei in G1 phase showed more profound shape fluctuations in the presence of GM6001 whereas S/G2 cell nuclei did not change their shape at all (Fig. 1J, right). In combination, these two methodologies complement each other for robust measurement of shape change applicable to all types of shape changes of biological objects over time and location. Together, associated with increased cell stiffness and vigorous deformation of the nucleus, G1 phase cells maintained migration speed in confinement, in contrast to migration-declining S/G2 phase or mixed G1/S/G2 cell populations (Fig. 1K).

.

Deformation-rounding cycles of the nucleus correlate with speed oscillations. To approach how deformation of the nucleus may support cell migration, the velocity of cell body, nucleus and the overall migration efficiency were recorded together with the nuclear morphology. To collagen lattices of decreasing pore sizes from around 100 to 10 µm^2 HT1080 cells responded

with a gradual decline of overall migration efficacy (Fig. 2A), consistent with our previous report [4]. High-resolution imaging revealed that, while the beeline representing overall migration gradually decreased, the speed of both nucleus and cell body remained unperturbed for all 3 pore conditions due to increasing oscillations (Fig. 2A), with the nuclear shape increasingly co-fluctuating (Fig. S4, middle column). These nucleus speed- and shape fluctuations corresponded to lateral 'swinging' of both nucleus and cell relative to the main axis of movement (Fig. 2B; Movie S4; Fig. S4, left column). In parallel, increasing nuclear deformation peaks preceded rapid nuclear rounding (Fig. 2B, grey filled nuclear outline; C, bottom). At oscillation peaks, nuclear shape change doubled (delta NII, 0.62 to 1.37; Fig. 2D), while the cell body remained elongated. Every nuclear rounding event was precisely accompanied by an up to 6-fold accelerated speed peak, each moving the nucleus by about half of its diameter forward (Fig. 2C, top; B, right). Accelerations versus remaining steps were in average 0.87 versus 0.15 μm/min, increasing overall migration of the nucleus by 50% (0.23 μm/min; Fig. 2D), as well as similarly the cell body. To support these findings in a migration model that enabled the visualization of the nucleus through pores of defined shape and size, a PDMS-based microdevice was used [37]. As in 3D collagen, migration through 10 μm^2 pores was followed by nuclear rounding and concomitant speed acceleration, whereas movement through 75 μm^2 pores lacked both, nuclear shape change and speed oscillation (Fig. 2E,F, Movie S5). Acceleration was several times higher as in collagen and possibly due to the higher elastic energy stored in the 5 μm^2-small nuclear deformation leading to a higher propulsive energy release into the barrier-free spacing following the tight pore. Taken together, cell passage through extracellular confinement coincides with nuclear deformation and is followed by piston-like acceleration of the nucleus together with transient rounding.

Saltatory propulsion of the rounding cell nucleus during migration in confinement is increased in G1 phase cells. Sustained migration in confined 3D environments in G1 cell cycle phase (Fig. 1J) is in line with a proposed promoting effect of chromatin condensation on cell migration [20,38], yet the mechanism of speed gain remained unclear. The above-described data suggest that the nucleus acts as obstacle during cell passage through small pores during phase (II), but in addition supports migration in phase IV, by pushing through the confinement and regaining roundish shape (Fig. 3A). To further characterize this last step of the transmigration process, we mapped nuclear speed and corresponding nuclear shapes (NII) over time, normalized to the moment of nuclear rounding ('phase IV peak') (Figs. 3B; S5A,B; Movies S2, S5). This

population analysis revealed, after a low-speed pore negotiation time, increased velocity peaks and, hence, speed oscillations for a population of single cells migrating through 10 μm^2 pores in engineered microdevices, whereas no peaks were generated in 75 μm^2 pores (Fig. 3C), consistent with data shown previously [37,39]. A similar step-wise peak acceleration, even though at lower velocity levels, was obtained with confinement in collagen (Fig. 3D). In G1 phase as compared to aggregated G1/S/G2 cells, speed peak events were again identified (Fig. S5A,B). The individual step-to-step speeds that G1/S/G2 cells performed during phase IV in confinement (blue box plot in Fig. 3E) were 2 times higher than the remaining migration steps, but were exceeded by around 25% in G1 phase nuclei (red box plot in Fig. 3E). Similarly, respective nuclear shape changes (delta NII, fluctuation) during phase IV peaks were 2-5 fold higher in confinement as compared to remaining events and to phase IV peaks in cells migrating in collagen in the presence of proteolysis (Fig. 3F,G). This principle held also true when relating shape change and speed in confinement for a single cell cycle progressing cell (Fig. S2C,D; Movie S1). Together, despite overall deceleration of cell migration in strongly confining environments, phase IV peaks support intermittent acceleration in G1/S/G2 interphase cells, which is further increased in G1 cell cycle cells only and associate with sustained migration of G1 phase cells in confinement. In contrast, spatially optimized environments allow for effective speed throughout all phases of nuclear deformation, resulting small or absent speed fluctuations.

Experimental chromatin decondensation reduces shape change and impairs migration. To directly test whether chromatin condensation can promote phase IV peaks for sustained cell migration in confinement, we treated cells with chromatin decondensating TSA. Consistent with nuclear swelling after chromatin decondensation [20] and confirmed here by a relatively low cell number, nuclear size in G1 phase cells increased after TSA pre-treatment in a dose-dependent manner, but not yet at a concentration of 100 ng/ml (Fig 4A). Accordingly, the nuclear elasticity decreased in a dose-dependent manner (from 1 to 0.6 kPa; Fig. 4B) [31], confirming data from HeLa cells [26]. Besides softening of the nucleus, TSA pre-treatment decreased migration speed in confinement by 33-80% (Fig. 4C) and speed correlated positively with nuclear stiffness (Fig. 4D). Congruent to lowered elasticity after chromatin decondensation, nuclei deformed more slowly during migration and their ability to change shape reduced by up to 60% compared to untreated control (Fig. 4E,F; Movie S6). Accordingly, as tested for 7-19 cells per condition, TSA treatment dampened phase IV accelerations (Fig. 4G), which were for a TSA concentration of 100 ng/ml not due to an increase in nuclear size, but due to a softened nucleus

and a possibly less dynamic microtubule network, leading to overall decreased migration rates in confinement. Treatment with 500 ng/mL TSA entirely inhibited speed fluctuations, which might, in addition, be due to the greatly increased nuclear size. Together, the data indicate that speed acceleration for effective migration in confinement requires chromatin condensation linked to high nuclear elasticity.

Besides chromatin condensation state, lamin A/C contributes to nuclear rigidity regulation. Downregulation of lamin A/C softens nuclei and supports migration rates through small pores ([28,40,41], own unpublished data), however its contribution to nuclear acceleration in phase IV remains unclear. Depletion of lamin A/C by RNAi reduced protein expression by 80% and nuclear stiffness by one third (our AFS analysis; data not shown), and associated with by 40% decreased 'phase IV' speed acceleration as compared to untreated cells (Fig. 4H). These data are in agreement with an increased deformation of the less elastic cell nucleus of lamin A/C-deficient cells as compared to the more elastic nucleus of control cells during and after passage of small pores [37]. The somewhat higher migration rates during the remaining phases I-III (see asterisk) are indicative for the previously shown increased migration rate of cells after lamin A/C downregulation in confinement [29,42]. Together, the data indicate that the nuclear deformation energy during high confinement is released into nuclear rounding during phase IV peaking and is proportional to lamin A/C expression and chromatin condensation mediated nuclear elasticity.

Discussion

Here we investigated 3D migration patterns of HT1080 fibrosarcoma cells in confining collagen lattices and microfabricated migration devices. The data reveal that cells and their nuclei do not migrate at a continuous speed, but undergo speed oscillations with velocities that increasingly deviate from beeline migration with confinement. Similar data of increasing nuclear oscillations in confinement presented by Yamada and colleagues [43] motivated a role of the cell nucleus in acting as a piston pressurizing the nucleo-anterior cell compartment and this way driving cell migration forward. Our findings complement these data well stating that nuclear fluctuations were caused by increasing nuclear deformations with confinement. This led to migration delay during the pore negotiation process in phases I-III, and was followed by a short speed-up phase during the last transmigration phase IV. Similar to speed oscillations, nuclear shape changes become higher in amplitude with increasing confinement, and this could be attributed to the postulated increasing nuclear recoil phenomenon in phase IV after passage

through a narrow pore [13]. Nuclear speed acceleration peaks were further responsive to the nuclear elasticity regulation during cell cycle progression as well as experimental chromatin decondensation and regulation of lamin A/C expression. Whereas with high stiffness and smaller size, i.e. during the G1 cell cycle phase, speed oscillations were increased, conditions that soften the nucleus, i.e. in S/G2 cell cycle phase, after experimental chromatin decondensation by TSA or by lamin A/C depletion, dampened periodic speed gain after pore passage.

Generally, processes connected with chromatin decondensation, mediated i.e. by cell cycle-progression or by respective pharmacological inhibitors, reduce migration, in accordance with a number of publications. Yano and coworkers tested migration of Fucci-positive MKN45 adenocarcinoma cell spheroids in confining Gelfoam® gels, and observed the least effective outward migration for S/G2/M phase cells [44]. Likewise, by applying a novel nano-printing technology to generate pores of defined areas on a smooth grated surface, S/G2 cell cycle cells showed less pore engagement and penetration efficiency as compared to M/G1 and G1 cell cycle phases [26]. Further, chromatin decondensation agents TSA as well as MTA, a general protein methyltransferase inhibitor, step-wise reduced B16 melanoma migration in a transwell membrane assay of 8 and 5 µm diameter pores [20], in accordance to our results at comparable pore size ranges in both 3D migration models. Of note, stathmin-regulated microtubule dynamics by acetylation / deacetyation is involved in 3D cell migration [45]. Tubulin deacetylation by HDAC6 is inhibited by TSA [46], and thus delayed migration rate is likely not only due to chromatin decondensation and softening, but also due to stabilization of microtubules. In their transwell assay, Gertlitz and colleagues observed that the migration rate through 8 µm diameter pores was reduced by TSA to around 75%, but through confining 5 µm pore diameters to 60% (TSA), and by MTA to 70% (8 µm) and 30% (5 µm pores). This data supports a dual effect of TSA, supported by MTA, namely on the cell's general migratory machinery as well as on the impact of nuclear deformation by confinement, affecting again migration.

In summary, we investigated the phenomenon of pore transmigration by speed fluctuation and nuclear recoil in the context of tumor cell invasion, but it will be interesting to test whether such oscillations during phases of active migration occur also in other biological contexts, i.e., during development, immune responses, or tissue repair. Together, this knowledge will have an impact on the general understanding of cell migration mechanisms in heterogenous environments.

Acknowledgements

We thank Peter Friedl, Mirjam Zegers and Tanmay Lele for their constructive feedback on this manuscript, Ben Fabry for helpful discussions on AFS analysis, Samuel Schmidt for technical help with flow cytometry, Sjoerd van Helvert for the generation of a fluorescent image atomic force micrsocope, and Esther Wagena for sorting the Fucci cells. We would like to acknowledge the Microscopic Imaging Centre core support at Radboudumc for the use of the combined AFS-confocal microscope (NWO Medium Sized Investment Grant 91110007) and Pathway spinning disk microscope. FWY, CV, AM and KW thank the Isaac Newton Institute for Mathematical Sciences for its hospitality during the program Coupling Geometric PDEs with Physics for Cell Morphology, Motility and Pattern Formation; EPSRC EP/K032208/1. This study was further supported by The Netherlands Organization for Scientific Research (NWO-VENI 680-47-421 to JtR; NWO-VIDI 917.10.364 to KW), the Leverhulme Trust Research Project Grant (RPG-2014-149 to FWY, CV and AM), the European Union's Horizon 2020 research and innovation program (Marie Sklodowska-Curie grant 642866 to AM), the National Science Foundation (CBET-125846 to JL) and the National Institutes of Health (U54CA210184 to JL). This work was performed in part at the Cornell NanoScale Facility (CNF), an NNCI member supported by NSF Grant NNCI-1542081.

Materials and Methods

Fucci plasmid construction and lentivirus preparation

Plasmids pFucci-G1-Kusabira Orange2 ("Fucci-red") and pFucci-S-G2-M-Amazi Green1 ("Fucci-green") [32] were purchased from MBL international. The IRES2 sequence was obtained by PCR using pIRES2-eGFP as template for primers 5'- GCG GAA TTC GTG TGT AGT ACT GTG TGT **GGA TCC GCC CCT CTC CCT C** -3' and 5'-GCG CTC GAG GTG TGT CCC GGG GTG TGT **CCA TGG TTG TGG CCA TAT TAT C** -3' (sequences in bold represent the IRES2 template-specific segments; underlined parts indicate restriction sites relevant for subsequent cloning steps). Obtained amplicon was digested with EcoRI and XhoI and inserted into pENTR-NotI/XhoI [47], creating pENTR-IRES2. An XmaI linker oligonucleotide (5'-TTA AGA CCC GGG TC-3') was heated and allowed to cool to room temperature to obtain a heteroduplex oligonucleotide with AflII-compatible ends, which was subsequently introduced in the AflII site in pFucci-G1-Orange2. Consequently, the sequence encoding human Cdt1 coupled to monomeric Kusabira-Orange2 could be excised using XmaI and NcoI and transferred into XmaI / NcoI digested pENTR-IRES2, resulting in pENTR-IRES2-Orange2. Finally, the part encoding human Geminin coupled to monomeric Azami-Green1 was excised from pFucci-S-G2-M-Green by using EcoRI and HpaI, and inserted into EcoRI/ScaI digested pENTR-IRES2-Orange2. The resulting plasmid pENTR-Fucci was used as donor in a Gateway® LR recombination reaction with destination vector pLenti6.2/V5-DEST™ (Invitrogen), yielding pLenti-Fucci; a single bicistronic lentiviral vector that results in dual-color fluorescentl labeling of live cells that are either in G1 (here referred to as Fucci-red) or S/G2/M (here referred to as Fucci-green) cell cycle phase. All constructs were sequence-verified.

Cell lines, lentivirus production, cell culture, and stable transduction of Fucci construct

The following cells were used: human HT1080-wild type fibrosarcoma cells (ACC315; DSMZ Braunschweig; [4]); HT1080 dual-color cells expressing cytoplasmic DsRed2 and nuclear histone-2B (H2B)–coupled EGFP [48]; HT1080 cells stably transfected with NLS-GFP [35] or H2B-mCherry; and HT1080 cells stably transfected with Fucci sensor. Cells were cultured in Dulbecco's modified Eagle medium (DMEM) supplemented with 10% fetal calf serum (FCS) containing L-glutamine (2 mM), sodium pyruvate (1 mM) and 100 U/mL penicillin, 100 µg/mL streptomycin and incubated at 37°C in a humidified 5% CO_2 atmosphere. Before cell experimentation, the detached and only loosely attached mitotic cells were washed away to only include interphase cells into all further assays.

For the generation of Fucci-positive HT1080 cells, recombinant lentiviral particles were produced, where in 10 cm dishes with 95% confluent HEK-293FT cell cultures were transfected overnight with JetPRIME reagent (Westburg) and a mixture of pLenti-Fucci plasmid and ViraPowerTM Packaging Mix (Invitrogen) according to the manufacturer's instructions. The following day, medium was refreshed and 48-72 h later virus-containing medium was harvested, passed through a 0.45 µm pore size filter and stored at -80°C until further use.
For stable transduction, HT1080 cells were seeded into 6 wells at 20-30% confluency, and on the next day medium was aspirated and 1 mL of viral-containing medium was drop-wise added to the cells and incubated overnight. On the following day the medium was replaced with fresh medium, followed by selection with 5 µg/mL blasticidine for 4-5 days after the transduction. Blasticidine was constantly kept on the cells during expansion, but removed 1-2 days prior to experimentation. Cells were sorted twice by flow cytometry for red or green fluorescence, resulting in a stable Fucci positive cell population not higher, however, of around 70%. Dynamic imaging of 2D cultures revealed an approximated 90% rate of an appropriate cell cycle-related temporal order of Fucci-colors (data not shown). Cell growth characteristics of HT1080 Fucci-positive cells related to values measured for HT1080 cells previously, with cell cycle times of ~5 h in G1-phase, ~9 h in S/G2-phase, and ~1.0 h in mitosis [33,49]. In addition, transfected cells remained functional with equal migration rates (0.2-0.4 µm/min) as compared to parental HT1080 cells [4]. These characteristics validate the applicability of the Fucci construct in HT1080 cells for investigating cell cycle-related functions.
For transient lamin A/C knockdown, cells were cultured in antibiotics-free supplemented DMEM in 6-well plates (each 250.000 cells) for 24 h. Cells were treated with a pool of small interfering (si) RNAs consisting of 4 single RNAs each and targeting expression of lamin A/C or non-targeting (NT) negative control (10 nM; on-target plus, SMARTpool; Dharmacon). The forward 21-nucleotide siRNA sequences for the NT control were 5-UGGUUUACAUGUCGACUAA-3, 5-UGGUUUACAUGUUGUGUGA-3, 5-UGGUUUACAUGUUUUCUGA-3, 5-UGGUUUACAUGUUUUCCUA-3; for si*LMNA* the forward sequences were 5-GAAGGAGGGUGACCUGAUA-3, 5-UCACAGCACGCACGCACUA-3, 5-UGAAAGCGCGCAAUACCAA-3, 5-CGUGUGCGCUCGCUGGAAA-3. siRNAs were transferred into cells with Dharmafect 4 transfection reagent according to the manufacturer's protocol and cultured with antibiotics-free DMEM for 48 h prior to characterization and functional studies. Lamin knockdown efficiency was determined by electrophoresis and western blot analysis from whole-cell lysates (62.5 mM

Tris-HCl; 2% w/v SDS; 10% glycerol; 50 mM DTT; 0.01% w/v bromophenol blue), followed by chemiluminescence detection (ECL detection kit; GE Healthcare) and densitometric analysis (Fiji ImageJ).

Analysis of the cell cycle stage by flow cytometry

Flow cytometry was performed to determine the relative DNA amount in respect to Fucci color within the cell population. Cultured HT1080 cells stably expressing Fucci marker were detached, re-suspended, and fixed with 500 µL 75% ice-cold ethanol for 1 h. Ethanol was carefully washed off and cells were incubated in 300 µL staining solution (1x PBS; 0.2 mg/mL RNase A, 1 µM DRAQ5) at 37°C for 30 min. Cells were measured on a CyAn ADP flow cytometer (Beckman Coulter) using spectral ranges 530/40 nm for Azami-Green1, 613/20 nm for Kusabira-Orange2 and 665/20 nm for DNA marker DRAQ5.

Probing nuclear mechanics by atomic force spectroscopy

Two days before AFS experimentation, 40.000 cells were seeded into a Willco dish in 1 mL DMEM/10 % FCS and incubated at 37°C in a humidified 5% CO_2 atmosphere. 12 h prior to the measurements, the medium was exchanged for 1 mL DMEM/10% FCS containing 10 mM HEPES (Gibco). Where indicated, cells were pre-treated with specified concentrations of histone deacetylase inhibitor trichostatin A (TSA, Sigma) 24 h before experimentation. Nuclear deformation measurements were performed using a Catalyst BioScope atomic force microscope (Bruker, Santa Barbara, CA, USA) combined with a 3-channel confocal microscope TCS SP5 II (Leica, Mannheim, Germany) for simultaneous brightfield and epifluorescence imaging through a Hamamatsu (ORCA-05G) camera and an air objective (20×, 0.70 NA). Flexible NP-S cantilevers modified with a 10 µm diameter bead were mounted, calibrated with the thermal noise method (te Riet et al., 2011), and subsequently located over the cell for repeated probing (3-5 times) at an approach and retraction rate of 10 µm/sec each with a pre-defined force of 15 nN. The registered force-distance (F-D) curves were transferred into force-indentation (F-δ) curves and used to calculate the penetration, stiffness, and dissipation of the nucleus [31]. The stiffness was calculated by using a custom algorithm written in IgorPro 6 (Wavemetrics) for fitting the F-δ curves with the Hertz model for spheres in contact with a flat surface (Digman et al., 2008). The energy dissipated during compression of the cell/ nucleus was derived from the integral between approach and retraction curve. In detail, a custom algorithm written in Matlab (MathWorks, Inc.) was used to determine the area underneath the approach and retraction curves. This area represents the energy needed to deform the nucleus; *i.e.* force (Newton) × distance

(meter) = energy (Nm = J). As a consequence, the dissipated energy during a probing cycle is $E_{dissipation} = E_{approach} - E_{retraction}$. The adhesion energy $E_{adhesion}$, measured as the area of the adhesion part in the retraction curve, was excluded because it is a measure of the stickiness of the bead probing the cell. The dissipation energy represents the difference between the energy to compress the nucleus and the energy 'recovered' upon retraction of the bead/cantilever, i.e., the energy dissipated or 'lost' in the nucleus due to plastic deformation. The dissipation energy is an indicator for the viscous component of the visco-elastic properties of the cell. The elastic part of the cell is represented by its penetrability.

3D collagen assays, time-lapse-microscopy and quantitative cell tracking

3D collagen lattices were prepared from acidic collagen solution (rat tail, Corning; or bovine, Advanced Biomatrix) supplemented with Minimal Essential Eagle's Medium (MEM; Sigma), HEPES and NaOH (for rat tail collagen; bicarbonate for bovine collagen) reaching a pH ~ 7.4, and mixed with the cell suspension to a final density of 200.000 cells/mL in collagen of indicated source and concentration. Usually, a concentration of 1.7 mg rat tail collagen/mL was used, unless indicated otherwise. Where indicated, cells were pre-treated with TSA for 24 h, and it was confirmed that cells remained viable, as judged by the absence of abnormal cell morphologies, or blebbing, and as further quantified by a propidium iodide assay, as detailed in [31]. A 100 µL cell-collagen mix was added to each well of a 96 well glass bottom plate, allowed to polymerize at 37°C in humidified 5% CO_2 atmosphere for 20-30 min, and was overlaid with medium. Where indicated, 5 µM GM6001 (Calbiochem) were added to both collagen and supernatant, and samples were monitored by temperature- and CO_2-controlled live microscopy over up to 24 h in 4 or 5 min frame intervals. Combined brightfield/ fluorescence imaging was performed on either an Okobab microscope (10×, NA 0.25, Nikon DiaPhot 300, a Hamamatsu ORCA AG CCD camera, an excitation and emission filter set for FITC and TRITC, and the 2D time lapse software Attovision), or on a spinning-disc confocal microscope (Pathway 855; BD Biosciences; 20x/0.40NA air objective; excitation filter sets of 488/10 and 548/20 nm, and emission filter sets of 520/35 nm and 600/15 nm). Life confocal microscopy for high resolution imaging of HT1080 cells was performed in time-lapse z-stack mode using a temperature- and CO_2 -controlled stage (37°C, 5%), and images were reconstructed as maximum intensity projections from all fluorescence and 2 reflection scans. Migration efficacy was quantified with the cell tracking program Autozell [version 1.0; Center for Computing and Communication Technologies (TZI), University of Bremen, Germany] of XY paths. The average speed per cell was calculated from

the length of the migration path divided by time. Only viable cells that showed dynamic changes in cytoplasmic extensions and retractions were tracked and included into the analysis.

Microfluidic migration devices

PDMS microfluidic devices were fabricated and used as previously described [37,50], with a migration chamber height of 5 µm and a pore width of either 2 or 15 µm, resulting in 10 and 75 μm^2 cross-sectional areas. In brief, the migration devices were coated with 50 µg/mL rat tail type-I collagen (BD Biosciences) in acetic acid (0.02 N) overnight at 4°C and rinsed with imaging medium to remove the coating solution. After loading the cells, devices were incubated for at least 3 hours to allow cell attachment before imaging. Microfluidic migration devices were imaged at 37°C on an inverted Zeiss Observer Z1 microscopes equipped with a CCD camera (Photometrics CoolSNAP KINO) using a 20×/NA 0.8 air objective. The image acquisition was automated through ZEN (Zeiss) software with imaging intervals of 4 and 5 min collecting images for DIC and GFP. Time-series images were stabilized using a custom-written MATLAB (Mathworks) script using features of the PDMS device as fiducials to compensate for the inaccuracy of the linear encoded microscope stage. Individual cells were tracked during the process of pore transmigration by using custom-developed MATLAB software [51].

Image analysis

For image analysis, in-focus nuclear areas and dynamic changes in nuclear shapes over time were analyzed using both the program Fiji ImageJ, or MATLAB with the in-house built-in software ITNA (Image and Trajectory Nuclear Shape Analysis; Sussex University). Image stacks were separated into individual channels, thresholded (mostly by automated thresholding algorithm Otsu) and nuclear outlines per time point were automatically collected. From these outlines, nuclear area, nuclear irregularity index (NII), and nuclear fluctuation were calculated. NII analysis was conducted by computing shape properties using the Imaging Processing Toolbox provided by MATLAB [52]. To calculate fluctuation, the two consecutive images were overlaid with their centroids and a 1°-stepwise full-circle (360°) rotation was performed to find the maximum overlap between these two shapes (Movie S3). The resulting fluctuation number was computed through

$$\text{Fluctuation} = \frac{A_1 + A_2 - 2(A_1 \cap A_2)}{A_1 + A_2},$$

where A_1, A_2 are the areas of the two consecutive nuclear shapes and $A_1 \cap A_2$ are the maximum intersections found through the rotation. The value range of this fluctuation number is $(0,1]$. The

value 0 indicates complete overlap of the nuclear shapes, while the value 1 implies no overlap at all. Phase IV events were defined as a combination of a NII value decrease (nuclear rounding) and a speed increase as a function of time and selected after visual inspection, and were depicted as speed as a function of shape change (delta NII).

Statistics

Statistical analysis was performed on independent samples with non-Gaussian distribution, using both the two-tailed non-paired Mann-Whitney test and the two-sample Kolmogorov-Smirnov test. Independency of G1 and S/G2 phase samples was confirmed by rejection of the null hypothesis (1% significance level; i.e. p-value = 0.01) and acceptance of the alternative hypothesis (99% confidence on the existence of a statistical significance between G1 and S/G2 phases).

Figure legends

Figure 1. Maintenance of migration through confining pores is associated with shape change of the small and rigid G1 cell cycle phase nucleus. (**A)** Sequence of a cell nucleus from a Fucci-positve HT1080 cell progressing through the cell cycle, as indicated by changing color coding over 4 hours. This sequence is part of Fig. S2 and Movie S1. **(B)** Quantification of cell deformation ('penetration') after 2 nN contact force by a bead-coupled cantilever connected to an atomic force microscope (quantified from the approach curve; Fig. S1D). N = 3; 25-32 cells per indicated cell cycle phase. **(C)** Top, example of collagen matrix (monitored by scanning electron microscopy as shown in [4]) showing small pore areas (confining; marked in pink), adjacent to large pores (marked in yellow). Bottom, cartoon depicting cell and nucleus in collagen of heterogenous, color-coded pore areas, including open space for translocation of cell and nucleus (asterisk). **(D-F)** HT1080- Fucci cells migrated in collagen (1.7 mg/ml) in the presence of MMP inhibitor GM6001 (except where absence of GM6001 is indicated), as monitored by pathway microscopy. (**D)** Examples of migrating cells at different indicated cell cycle phases. (**E)** Averaged migration speed of single cells from Fucci-red or -green populations from movies of 5-24 h length at indicated conditions. Because the S-start phase covers a short, around 2 hour, time period, from here on and in all further experiments G1 phase cells were compared with S/G2 cells only. N = 2-3; 40-65 cells per condition. **(F)** Nuclear segmentation of migrating HT1080-Fucci cells. Time in minutes as indicated. **(G-J)** Nuclear shape analysis. **(G)** Top, schematic illustration of the components used for the calculation of the nuclear irregularity index (NII). Adapted from [36]. Bottom, calculation of all components that describe a circle, resulting in a NII of 2.2146. (**H)** Mean NII values per cell were computed and calculated from each nuclear shape sequence over time. (**I)** Left, scheme for calculation of the difference between subsequent NII's as delta NII, where rapid shape change of the nucleus results in a high delta NII value. Right, mean values of delta NII from each nuclear shape sequence over time. (**J)** Nuclear fluctuation analysis, sketching the analysis procedure (left), and mean values of the fluctuations from each nuclear sequence to the next (right). In **(H-J)**, mean value per cell over 36-316 minutes; n = 3; 38 and 29 cells per G1 and S/G2 phase, respectively. **(K)** Summary of speed as a function of nuclear shape change (delta NII) in optimal and confining collagen conditions (data are from **(E,I)**. Dots connected by red line represent G1 cycle cells; by green line, S/G2 cycle cells; by black line, G1 and S/G2 cycle cells together. **(B,E,H,I,J)** Black horizontal lines, boxes and whiskers show the medians, $25^{th}/75^{th}$, and $5^{th}/95^{th}$ percentile (**B,** $10^{th}/90^{th}$ percentile), and ***, $P \leq 0.001$; **, $P \leq 0.01$; *, $P \leq 0.05$; ns, non-significant (Mann Whitney test). All image bars, 10 µm.

Figure 2. Speed oscillation and rapid nuclear rounding during cell migration in confining pores. HT1080 fibrosarcoma cells moved either in collagen **(A-D)** or in a synthetic microdevice **(E,F**). **(A)** Cells migrated in collagen of increasing density and the absence or presence of GM6001 as indicated, resulting in depicted decreasing effective pore areas (top; [35]). From each 3 cells, speed of nucleus and cell body was quantified from the migration tracks from the center of the nucleus as well as the cell body that often demonstrated synchronous speed peaks. In addition, the overall migration speed was measured as 'beeline' between the center of nuclei from the first and last image as depicted in Fig. S4 and normalized over 55 min. **(B-D)** Oscillatory speed peaks of the cell and nucleus during migration coincide with nuclear rounding. **(B)** Upper row, left, sequences of HT1080 dual-color cell moving within high density bovine collagen (3.3 mg/ml) monitored by confocal microscopy at 37°C at 5 min intervals [13]. White dots at first and last image and dotted white line indicate position and beeline of the migrated nucleus. Lower row, left, outlines of the nucleus generated from H2B-eGFP signal, with centroids (blue dots) and centroid-connecting movement trajectories in red. Long trajectories indicated in cyan, green and orange and by arrows represent peak movements, and respective nuclear roundings are marked by colored outline and grey area in the outline. Right, overlay of the first and all rounded outlines, and trajectory of the nucleus over 5 hours (corresponding to Movie S4). **(C)** Upper graph, step-to-step and average speed quantification from the movement trajectories of moving cell body and nucleus from (B), as well as the beeline of the migrated nucleus. Repeated speed peaks ('oscillations') of the nucleus are indicated by respective colored dots. Lower graph, corresponding repeated phases of nuclear rounding measured as NII, indicated by respective colors and arrowheads. **(D)** Speed as a function of delta NII per time step (=dot) of the moving nucleus shown in (B), and quantified in (C). Top right, note the link between high speed of forward movement (peak oscillations) and rapid rounding of the nucleus, shown by dots in colors respective to (B,C). All numbers and dotted lines in black and green indicate medians of speed and delta NII, respectively, for either colored oscillation peaks or all remaining dots. Dotted line and number in pink indicate speed median from all dots. **(E)** Migration in microdevice of 10 and 75 μm^2 pore areas **(**corresponding to Movie S5, 2. part). Left, upper row, sequence of migrating cell over indicated time. White arrowhead, deformed nucleus in pore. Arrowhead in cyan indicates rounding. Lower row, nuclear outlines with centroids as blue dots and trajectories in red. Arrow indicates long trajectory in cyan that corresponds to nucleus rounding. Right, kymogram, visualizing rapid forward movement (arrow) after transmigration of narrow pore. **(F)**

Speed and corresponding NII, with color coding matching imaging sequence. Bottom, speed - nuclear shape change relationship; number in green, delta NII value for peak oscillation. Reprinted modified images in (B) are with permission from Elsevier [13]. All image bars, 10 μm.

Figure 3. Characterization of 'phase IV' peak events. (A) Concept of nuclear deformation phases during cell migration through narrow pores. Adapted from [13]. **(B)** Cartoon depicting selection scheme for phase IV speed peak values connected to nuclear rounding as shown in **(C)** and **(D)**. **(C)** Speed of nuclei before (phase I and II), during (phase III) and after (phase IV) transmigration of pores of 75 μm^2 (grey) and 10 μm^2 (cyan) cross-section from microdevice. Vertical dotted line indicates time point when nuclei passed the center of the pore (see inset), and grey shadowed area indicates phase IV. Solid lines represent mean, and shadowed colored area +/- SEM. 21 cells per condition, n=3. P value was calculated for speed peaks at 5 min after pore passage of 10 μm^2 as compared to data from 75 μm^2 pores. Asterisk indicates decreased speed during passage of small as compared to big pores. **(D)** Quantification of phase IV-speed peaks in collagen of decreasing effective pore size. The onset of each speed peak event was normalized to 0 min (dotted vertical line) and calculated based on speed increase in the moment of nuclear rounding (see black boxes in Fig. S4,A-C, middle panels; S5A,B). N = 1-3; graphs are superimposed from 8-25 respective events from each 5-8 cells per condition monitored at high resolution; mean (colored solid lines) +- SEM (shadowed colored areas). Grey shadowed area indicates phase IV event. Values of the peak speeds are also displayed as box plots. P value was calculated for speed peaks at 4 min after pore passage, as compared to data from 1.7 mg/mL collagen in the absence of GM6001. **(E-G)** Depiction and analysis of either phase IV (strong colors) or all remaining non-phase IV events (light colors) from G1 cell cycle phase cells (pink and grey), or mixed G1/S/G2 cell cycle cells (blue and grey; **E, left**) after migration in collagen **(**1.7 mg/mL) and GM6001 where indicated. Analysis of **(E)** speed, **(F)** delta NII as shown in Fig. 1I, and **(G)** nuclear fluctuation, as shown in Fig. 1J, with the difference that instead of a mean value per cell over time, values from each time point of a moving cell were defined and separated into phase IV peak and remaining events selected as in (B). The single dots in (**F,G**) depict the medians from the G1 phase cell results from Figs. **1I,J**. (**E**, left; G1/S/G2 cells) N=1-3; 50-79 phase IV peak events and 363-387 remaining events were analyzed from nuclear sequences of 16-21 cells per condition. **(E,** right **– G**; G1 cells**)** N=1-3; 24-67 phase IV peak events and 180-424 remaining events were analyzed from nuclear sequences of 8-13 cells per condition. In **(D-G)**, data are depicted as horizontal lines, boxes and whiskers for medians,

$25^{th}/75^{th}$, and $5^{th}/95^{th}$ percentile. For all experiments, ***, $P \leq 0.001$; **, P, <0.01; ns, non-significant (both Mann Whitney and Kolmogorow test).

Figure 4. Altered stiffness, migration and reshaping of HT1080 cells and nuclei after TSA treatment or lamin A/C downregulation. Cells were pre-treated with indicated TSA concentrations or DMSO alone (indicated as 0 ng/mL TSA), and were either measured for elastic modulus **(B)** or migrated in collagen (1.7mg/ml) in the presence of GM6001**(A,C-F)**. For all TSA experiments, except in **(B)** and **(C)**, Fucci cells were used and G1 phase cells only were selected for analysis. **(A)** Nuclear areas after pre-treatment with TSA in collagen. Horizontal black lines show the medians. N=1; 5-19 cells per TSA concentration. **(B)** Calculated stiffness at 1.5 nN contact force by bead-coupled cantilever probing using atomic force microscopy. 14-37 cells per condition; n = 1-3. **(C)** Mean cell migration efficacy per cell over 24 h with increasing concentrations of TSA as compared to DMSO control. Cells that underwent mitosis during the recording were excluded from the analysis. N = 3; 66-90 cells per condition. **(B,C)** Horizontal black lines, boxes and whiskers show the medians, $25^{th}/75^{th}$, and 10^{th} and 90^{th} **(B)** and 5th/95th **(C)** percentile. **(D)** Correlation of stiffness with migration efficacy, using the medians and whiskers from (A,B). $R^2 = 0{,}92$. **(E)** Representative segmented nuclear sequences from migrating G1 phase (Fucci-red) cells at indicated time steps, in correspondence to Movie S6. Arrows indicate phase IV peak events based on speed increase and concomitant nucleus rounding. Bar, 10 μm. **(F)** Nuclear shape change during migration by TSA. Mean delta NII per cell migrating over 0.3 to 10 h. Zero means no changes between subsequent nuclear shapes. 5-19 cells per condition, shown as dots. Horizontal black lines show the medians. **(G)** Speed peaks, as in Fig. 3C, at indicated TSA concentrations. Graphs are superimposed from 22-38 respective events from each 7-19 cells per condition; n = 1. Mean (colored solid lines) +- SEM (shadowed colored areas). Asterisk indicates decreased nuclear speed after TSA treatment before phase IV peak. **(H)** Left, lamin A/C expression intensity by western blot after transient downregulation by indicated siRNA (each 10 nM). Right, speed peaks in cells treated with non-targeting and LaminA/C siRNA after transmigration of 10 μm^2 pore. Asterisks indicate increased nuclear pore negotion speed after silamin A/C treatment before phase IV peak event. Each 21 cells per condition. **(G; H, right)** Dotted vertical lines, speed peak at nuclear rounding; grey-shadowed areas, phase IV events. ***, $P \leq 0.001$; **, $P \leq 0.01$; *, $P \leq 0.05$; non-significant. n.s.; (**A,B,C,F,** Mann-Whitney test; **G, H** Students t-test).

Supplementary figure legends

Figure S1. Characterization of HT1080 cells after stable transduction with Fucci vector. **(A)** Cartoon of fluorescence ubiquitination-based cell cycle sensor Fucci, adapted from the ThermoFisher Scientific website, demonstrating how cell cycle stages can be optically separated by color coding. The Fucci biosensor exploits the cell cycle-regulated proteolysis of Cdt1 and Geminin, two proteins involved in licensing of replication origins [53]. Ctd1- Kusabira-Orange2 expression is assigned to G1 phase (Fucci-red), which is degraded by the ubiquitin proteasome system when S phase is commencing. Reciprocally, Geminin-Azami-Green1 expression is assigned to the S, G2, and M phases (Fucci-green) and is rapidly broken down upon exit of mitosis. Consequently, cells express both colors (Fucci-yellow) only during the early S phase. Because before cell experimentation the detached and only loosely attached mitotic cells are washed away, green colored cells are in the following termed S/G2. (**B)** Distribution of cell cycle stages in HT1080 cells. Top, percentage of G1, S, and S/G2 phase distributions from 387 adherent cells from 2D cell culture. Bottom, flow cytometric analysis of an ethanol-fixed cell population. Chromosomal complementation is displayed as diploidic (2N) that refers to cells in G1 phase whereas the tetraploidic (4N) cell population refers to cells in S/G2 phase. Cells in S-start phase are distributed in between 2N and 4N, as chromatin duplication is not yet completed. Numbers within compartments are estimated fractions in percent. Back-gating confirmed that S/G2 Fucci-green cells (small peak in green) fill part of the 4N-related peak meaning that they have completed DNA duplication. Dotted pink line indicates the anticipated Fucci-red cell population, as Cdt1-Kusabira-Orange2 fluorescence was lost during fixation. (**C)** Nuclear areas in G1 and S/G2 phase, measured from cells either plated on glass or in collagen. Median, horizontal line. N=2, 51 cells per cell cycle phase (on glass); n=3; 38 and 29 cells per cell cycle phase (in collagen). **(D)** Principle of AFS-force measurements (see [31]). Image and cartoon show that prior to a measurement, a 10 µm-diameter-sized bead immobilized on an cantilever was positioned above the center of the nucleus. Cells were selected by epifluorescence microscopy mode for suitability by morphology and cell cycle phase. After cantilever-mediated approach, compression, and retraction from the cell, the resulting force-distance curves were plotted (graph). Image bar, 20 µm. **(E)** Relative dissipation energy, derived as the area between approach (E_{appr}) and retraction (E_{diss}), and divided by the energy needed to deform the nucleus (E_{appr}). A value of 0 represents a purely elastic nucleus where approach and retraction curves overlap (the nucleus recoils completely, and all of the compression energy is recovered);

increasing values indicate increasingly viscous material behavior, including plastic deformation and viscous dissipation of the energy required to compress the nucleus (the nucleus remains partially deformed after the cantilever has been retracted). N = 3; 30-32 cells per condition. Black horizontal lines, boxes and whiskers show the medians, 25^{th}/75^{th}, and 10^{th}/90^{th} percentile. **(F)** Cartoon depicting how the disspation energy was extracted from force-distance curves after a compression-relaxation cycle of a cell when probed by a bead-functionalized cantilever. **(G)** Two example curves of each nucleus in G1-phase and in S/G2-phase show the differences in dissipation indicative for the significant difference found in **(E)**. ***, $P < 0.001$; **, $P < 0.01$; ns, non-significant (Mann-Whitney test).

Figure S2. Analysis of cell cycle transition-related nuclear parameters by imaging of a single HT1080-Fucci cell. (A) Image sequence from a single migrating cell in collagen in the presence of GM6001, demonstrating a single cell cycle transition over 4 hours (see Fig. 1A and Movie S1). Upper lanes, single red, single green and merged channels. Lowest lane, nuclear outline produced in Fiji ImageJ by Otsu-thresholding. (**B,C)** Quantification of indicated parameters showing each of the gradual change over 4 hours. The up- or downwards trend is indicated by black lines obtained by the trendline function in Fiji, and this trend as well as all quantifications coincide with population data in Figs. 1 and S1. Pink, yellow and green colors indicate the different cell cycle phases as marked in A. **(B)** Quantification of increasing nuclear area during G1 to S/G2 phase transition. Grey shadowed area, out of focus region as marked in (A). (**C)** Top graph, speed fluctuation of cell body. All other graphs, from second top to bottom, quantification of speed and morphometric parameters (NII, delta NII, and fluctuation) of the nucleus, all decreasing from G1 to S/G2 phase. Speed- nuclear shape change relationship for identification of phase IV events are marked by vertical pink lines, and are shown as colored path segments in Movie S1. **(D)** Depiction of phase IV events (encircled) versus all events, color-coded per cell cycle phase. Quantification coincides with population data in Figs. 2D and S5C.

Figure S3. Depiction of the advantage of nuclear irregularity index versus nuclear rounding calculation. (A) Left, depiction of nuclei from 5 cells carrying the Fucci construct. Right, graphs show calculation of nuclear shape change for a nucleus from a migrating cell over time, using NII (formula introduced in Fig. 1G) and roundness. Colored arrowheads indicate nucleus rounding. Top, value for a circle is indicated; bottom, area in light grey indicating around 50% roundness values that oscillate around 1 [see explanation in **(D)**]. Thus, when a

relatively low-resolution image is used, a single shape property like roundness can be unreliable, but NII with a combination of four shape properties is still robust, indicating the expected shape changes more clearly. **(B)** Left, depiction of nucleus from high-resolution imaging (Fig. 2B); right graphs, depicting NII and roundness and indicating convincing agreement. **(C)** Mean nuclear shapes calculated from single G1 and S/G2 phase cells monitored at low resolution. Difference is significant after calculation of NII, but not after calculation of roundness. Area in light grey indicates roundness values oscillating around 1. Because of roundness' unreliability in low resolution imaging, NII was chosen over roundness. **(D)** Schematic illustration of how the nucleus perimeter was calculated within the calculation of roundness. Rather than a simple edge count method, a polygonal approximation was implemented. This approximation took into account the inward and outward corners, and straight lines. Different weights were assigned, since a digital representation of a shape can only be pixelated without smooth curves. Such an approximation with enough pixels improves the calculation of the perimeter, whereas less pixels entail an under-estimation of the perimeter with a value below 1. All image bars, 10 μm.

Figure S4. Speed peaks and rounding of the nucleus increase with confinement. HT1080 cells migrated in collagen of increasing indicated concentrations and the absence or presence of GM6001 (sequences and values correspond to Fig. 2A). **(A-C) Left column,** upper rows, sequences of migrating cells over indicated time periods and in indicated colors for cell body (DsRed2 or transmission signal), nucleus (H2B-eGFP, H2B-mCherry or NLS-GFP) and collagen reflection signal. Color-coded arrowheads indicate rounding even if marginal. Lower rows, nuclear outlines or segmentations, respectively, with centroids as blue dots and trajectories in red. Arrows indicate long, colored trajectories that correspond to nucleus rounding indicating phase IV peak events. **(B,C)** Dotted rectangle, inset where nucleus in bottom row was enlarged from. **(C)** White arrows, detachment of cell rear corresponding to velocity peak and rounding of nucleus. All bars, 10 μm. **Middle column,** speed patterns of nuclei (top), and corresponding NII value, all with color coding matching events in imaging sequences. Speed peaks that associate with decreasing NII values ('phase IV peak events') are indicated by colored dots and grey areas, and representative speed peak sizes are indicated by length of black boxes. **Right column**, speed as a function of delta NII, where values that relate to color-coded speed peaks/nuclear rounding are encircled, and numbers in green, median value of respective delta NII. Part of the image sequence from **(C)** is reproduced from [35].

Figure S5. Selection and depiction scheme of phase IV speed peak/ nuclear rounding events. **(A)** Imaging sequence and segmentation from a representative G1 phase HT1080-Fucci cell nucleus migrating in collagen (1.7 mg/ml) in the presence of GM6001. **(B)** Analysis of the nuclear parameters speed and NII, and simultaneous display over time to demonstrate how phase IV nuclear events were selected according to when a speed peak was associated with a decrease of NII from one timestep to the next. Phase IV events are marked by colored dots and vertical pastel-colored stripes, and the corresponding rounded nuclear shapes in **(A)** are marked by red-colored outline. **(C)** Phase IV (pink dots) and non-phase IV (black dots) events from G1 phase cell nuclei from cells migrating in collagen (1.7 mg/mL) and in the absence and presence of GM6001, where speed is shown as a function of delta NII values per time step (data points and cell numbers correspond to Fig. 3E right;F). Colored ellipses indicate increased shape change of phase IV events in right graph as compared to left graph.

Movie legends

Movie S1. Spontaneous migration of mesenchymal HT1080-Fucci cells over different interphase cell cycle phases. Migrating HT1080-Fucci cells in 3D collagen in the presence of GM6001 were imaged by pathway microscopy at 37°C. Fluorescently labeled nuclei (**middle panel**) were overlaid with brightfield signal showing polarized cell bodies within 3D collagen in different layers (**left panel**). Marked cell in left-upper corner migrated to the right-lower corner while it transited from G1 (pink) to S-Start (yellow) and S/G2 (green) cell cycle phase. In cell track, segments of phase IV peak step-to-step distances, when appearing with nuclear rounding (see colored dots and arrowheads Fig. S2C), were marked in respective Fucci color. **Right panel,** respective crops from the nucleus of the marked cell during cell cycle transition, with forward moving tip of nucleus being directed towards the bottom, together with Otsu-segmented outline, complementary to Fig. 1A and S2A, and used for quantifications in Fig. S2B-D. Time as indicated. Bar, 50 μm.

Movie S2. Phase IV peak events in migratory G1 phase HT1080 cells. Segmentation of in focus-HT1080 cell nuclei from G1 (as well as S/G2) phase during cell migration in collagen in the presence of GM6001, cropped from overview image sequences such as Movie S1. In the first part of the movie only the nuclear morphologies are shown, whereas in the second part centroids per segmented nucleus are shown in blue, together with centroid-connecting cell tracks where

‘phase IV events’ are marked by pink (or green) track segments. G1 phase nucleus sequence marked with asterisk is displayed in Fig. S5A. Time as indicated.

Movie S3. Illustration of the nuclear shape rotation method for fluctuation analysis. The two left columns show the previous and current frames of a sequence separated by 4 minutes each. The second column to the right shows the anticlockwise rotation in 1 degree steps of the ‘current’ over the ‘previous’ segmented frame. Non-overlapping areas are shown in pink and green. The right column reflects the ‘best fit’ with maximum overlap of the 2 shapes, where 0 means complete overlap. Note that the ‘best fit’ is updated whenever a new maximum overlap is found during the rotation. This analysis tool corresponds to fluctuation analysis used in Fig. 1J.

Movie S4. HT1080 dual-color cell in dense collagen: oscillatory migration and repeated rapid rounding of the nucleus. Cell migrates within bovine collagen (3.3 mg/ml; reflection signal) by shape change of cell body (DsRed2) and nucleus (H2B-eGFP), as imaged by confocal microscopy at 37°C over 5 hours (left). Each computed outline of cell body and nucleus contains a centroid (blue) that progressively forms migration paths (red). Long path segments marked in cyan, green, orange and yellow color in both cell body and nucleus associate with rapid nuclear rounding (grey filling) and represent ‘phase IV peak events’. Progressing outline of cell body stalls at 135 min as pseudopod leaves image field (black arrowhead). Nucleus outlines presented either as simple progressing (middle), progressive overlay of outlines (second to the right) and as overlay of grey rounded areas after oscillatory velocity peaks. Movie corresponds to Fig. 2B. Time as indicated. Bar, 10 μm.

Movie S5. Migration of HT1080 cells through synthetic microdevice. Cells transfected with NLS-GFP migrated through indicated 10 μm^2 and 75 μm^2 pores of a microdevice over 9 h (first movie part) or around 1 h (second movie part). Green, NLS-GFP signal; transmission, PDMS pillars and cell bodies. Arrowheads indicate examples of nuclear passage through pore center, of which events were used for Fig. 3C (first movie part) or Fig. 2E (second movie part, with long phase IV-associated trajectory in cyan).

Movie S6. TSA reduces cell migration efficacy and nuclear shape change. HT1080 G1 phase (Fucci-red) cells, after pre-treatment by DMSO or TSA moved in collagen in the presence of GM6001. Note the size increase of the nucleus after pre-treatment by 500 ng/mL TSA.

Comparison of the original fluorescent nuclear shapes (left column) with thresholded segmented counterparts (middle) and outlines (right) illustrate segmentation quality used for this study. Complementary with Fig. 4E. Time as indicated.

References

1 Fidler, I. J. The pathogenesis of cancer metastasis: the 'seed and soil' hypothesis revisited. *Nature reviews. Cancer* **3**, 453-458, doi:10.1038/nrc1098 (2003).

2 Paul, C. D., Mistriotis, P. & Konstantopoulos, K. Cancer cell motility: lessons from migration in confined spaces. *Nat Rev Cancer* **17**, 131-140, doi:10.1038/nrc.2016.123 (2017).

3 Weigelin, B., Bakker, G.J., Friedl, P. Intravital third harmonic generation microscopy of collective melanoma cell invasion -Principles of interface guidance and microvesicle dynamics. *IntraVital* **1**, 1-12 (2012).

4 Wolf, K. *et al.* Physical limits of cell migration: control by ECM space and nuclear deformation and tuning by proteolysis and traction force. *J Cell Biol* **201**, 1069-1084, doi:10.1083/jcb.201210152 (2013).

5 Lammerding, J. Mechanics of the nucleus. *Compr Physiol* **1**, 783-807, doi:10.1002/cphy.c100038 (2011).

6 Liu, H. *et al.* In situ mechanical characterization of the cell nucleus by atomic force microscopy. *ACS Nano* **8**, 3821-3828, doi:10.1021/nn500553z (2014).

7 McGregor, A. L., Hsia, C. R. & Lammerding, J. Squish and squeeze-the nucleus as a physical barrier during migration in confined environments. *Curr Opin Cell Biol* **40**, 32-40, doi:10.1016/j.ceb.2016.01.011 (2016).

8 Fu, Y., Chin, L. K., Bourouina, T., Liu, A. Q. & VanDongen, A. M. Nuclear deformation during breast cancer cell transmigration. *Lab Chip* **12**, 3774-3778, doi:10.1039/c2lc40477j (2012).

9 Thiam, H. R. *et al.* Perinuclear Arp2/3-driven actin polymerization enables nuclear deformation to facilitate cell migration through complex environments. *Nat Commun* **7**, 10997, doi:10.1038/ncomms10997 (2016).

10 Jayo, A. *et al.* Fascin Regulates Nuclear Movement and Deformation in Migrating Cells. *Dev Cell* **38**, 371-383, doi:10.1016/j.devcel.2016.07.021 (2016).

11 Wu, J. *et al.* Actomyosin pulls to advance the nucleus in a migrating tissue cell. *Biophys J* **106**, 7-15, doi:10.1016/j.bpj.2013.11.4489 (2014).

12 Thomas, D. G. *et al.* Non-muscle myosin IIB is critical for nuclear translocation during 3D invasion. *J Cell Biol* **210**, 583-594, doi:10.1083/jcb.201502039 (2015).

13 Friedl, P., Wolf, K. & Lammerding, J. Nuclear mechanics during cell migration. *Curr Opin Cell Biol* **23**, 55-64, doi:10.1016/j.ceb.2010.10.015 (2011).

14 Fedorchak, G. R., Kaminski, A. & Lammerding, J. Cellular mechanosensing: getting to the nucleus of it all. *Progress in biophysics and molecular biology* **115**, 76-92, doi:10.1016/j.pbiomolbio.2014.06.009 (2014).

15 Swift, J. *et al.* Nuclear lamin-A scales with tissue stiffness and enhances matrix-directed differentiation. *Science* **341**, 1240104, doi:10.1126/science.1240104 (2013).

16 Kaufmann, A., Heinemann, F., Radmacher, M. & Stick, R. Amphibian oocyte nuclei expressing lamin A with the progeria mutation E145K exhibit an increased elastic modulus. *Nucleus* **2**, 310-319, doi:10.4161/nucl.2.4.16119 (2011).

17 Schape, J., Prausse, S., Radmacher, M. & Stick, R. Influence of lamin A on the mechanical properties of amphibian oocyte nuclei measured by atomic force microscopy. *Biophysical journal* **96**, 4319-4325, doi:10.1016/j.bpj.2009.02.048 (2009).

18 Pajerowski, J. D., Dahl, K. N., Zhong, F. L., Sammak, P. J. & Discher, D. E. Physical plasticity of the nucleus in stem cell differentiation. *Proc Natl Acad Sci U S A* **104**, 15619-15624, doi:10.1073/pnas.0702576104 (2007).

19 Stephens, A. D., Banigan, E. J., Adam, S. A., Goldman, R. D. & Marko, J. F. Chromatin and lamin A determine two different mechanical response regimes of the cell nucleus. *Mol Biol Cell* **28**, 1984-1996, doi:10.1091/mbc.E16-09-0653 (2017).
20 Gerlitz, G. & Bustin, M. Efficient cell migration requires global chromatin condensation. *J Cell Sci* **123**, 2207-2217, doi:10.1242/jcs.058271 (2010).
21 Sarma, K. & Reinberg, D. Histone variants meet their match. *Nat Rev Mol Cell Biol* **6**, 139-149, doi:10.1038/nrm1567 (2005).
22 Hizume, K. *et al.* Nano-scale analyses of the chromatin decompaction induced by histone acetylation. *Arch Histol Cytol* **73**, 149-163 (2010).
23 Unnikrishnan, A., Gafken, P. R. & Tsukiyama, T. Dynamic changes in histone acetylation regulate origins of DNA replication. *Nat Struct Mol Biol* **17**, 430-437, doi:10.1038/nsmb.1780 (2010).
24 Bartova, E., Krejci, J., Harnicarova, A., Galiova, G. & Kozubek, S. Histone modifications and nuclear architecture: a review. *J Histochem Cytochem* **56**, 711-721, doi:10.1369/jhc.2008.951251 (2008).
25 Toth, K. F. *et al.* Trichostatin A-induced histone acetylation causes decondensation of interphase chromatin. *J Cell Sci* **117**, 4277-4287, doi:10.1242/jcs.01293 (2004).
26 Panagiotakopoulou, M. *et al.* A Nanoprinted Model of Interstitial Cancer Migration Reveals a Link between Cell Deformability and Proliferation. *ACS Nano* **10**, 6437-6448, doi:10.1021/acsnano.5b07406 (2016).
27 Chalut, K. J. *et al.* Chromatin decondensation and nuclear softening accompany Nanog downregulation in embryonic stem cells. *Biophys J* **103**, 2060-2070, doi:10.1016/j.bpj.2012.10.015 (2012).
28 Harada, T. *et al.* Nuclear lamin stiffness is a barrier to 3D migration, but softness can limit survival. *The Journal of cell biology* **204**, 669-682, doi:10.1083/jcb.201308029 (2014).
29 Davidson, P. M., Denais, C., Bakshi, M. C. & Lammerding, J. Nuclear deformability constitutes a rate-limiting step during cell migration in 3-D environments. *Cell Mol Bioeng* **7**, 293-306, doi:10.1007/s12195-014-0342-y (2014).
30 Greiner, A. M. *et al.* Multifunctional polymer scaffolds with adjustable pore size and chemoattractant gradients for studying cell matrix invasion. *Biomaterials* **35**, 611-619, doi:10.1016/j.biomaterials.2013.09.095 (2014).
31 Krause, M., Te Riet, J. & Wolf, K. Probing the compressibility of tumor cell nuclei by combined atomic force-confocal microscopy. *Phys Biol* **10**, 065002, doi:10.1088/1478-3975/10/6/065002 (2013).
32 Sakaue-Sawano, A. *et al.* Visualizing spatiotemporal dynamics of multicellular cell-cycle progression. *Cell* **132**, 487-498, doi:10.1016/j.cell.2007.12.033 (2008).
33 Marcus, J. M., Burke, R. T., DeSisto, J. A., Landesman, Y. & Orth, J. D. Longitudinal tracking of single live cancer cells to understand cell cycle effects of the nuclear export inhibitor, selinexor. *Sci Rep* **5**, 14391, doi:10.1038/srep14391 (2015).
34 Wolf, K. *et al.* Multi-step pericellular proteolysis controls the transition from individual to collective cancer cell invasion. *Nat Cell Biol* **9**, 893-904, doi:10.1038/ncb1616 (2007).
35 Denais, C. M. *et al.* Nuclear envelope rupture and repair during cancer cell migration. *Science* **352**, 353-358, doi:10.1126/science.aad7297 (2016).
36 Filippi-Chiela, E. C. *et al.* Nuclear morphometric analysis (NMA): screening of senescence, apoptosis and nuclear irregularities. *PLoS One* **7**, e42522, doi:10.1371/journal.pone.0042522 (2012).

37 Davidson, P. M., Sliz, J., Isermann, P., Denais, C. & Lammerding, J. Design of a microfluidic device to quantify dynamic intra-nuclear deformation during cell migration through confining environments. *Integr Biol (Camb)* **7**, 1534-1546, doi:10.1039/c5ib00200a (2015).
38 Gerlitz, G. & Bustin, M. The role of chromatin structure in cell migration. *Trends Cell Biol* **21**, 6-11, doi:10.1016/j.tcb.2010.09.002 (2011).
39 Lautscham, L. A. *et al.* Migration in Confined 3D Environments Is Determined by a Combination of Adhesiveness, Nuclear Volume, Contractility, and Cell Stiffness. *Biophys J* **109**, 900-913, doi:10.1016/j.bpj.2015.07.025 (2015).
40 Yadav, S. K. *et al.* Elevated nuclear lamin A is permissive for granulocyte transendothelial migration but not for motility through collagen I barriers. *J Leukoc Biol*, doi:10.1002/JLB.3HI1217-488R (2018).
41 Rowat, A. C. *et al.* Nuclear envelope composition determines the ability of neutrophil-type cells to passage through micron-scale constrictions. *J Biol Chem* **288**, 8610-8618, doi:10.1074/jbc.M112.441535 M112.441535 [pii] (2013).
42 Infante, E. *et al.* LINC complex-Lis1 interplay controls MT1-MMP matrix digest-on-demand response for confined tumor cell migration. *Nat Commun* **9**, 2443, doi:10.1038/s41467-018-04865-7 (2018).
43 Petrie, R. J., Harlin, H. M., Korsak, L. I. & Yamada, K. M. Activating the nuclear piston mechanism of 3D migration in tumor cells. *J Cell Biol* **216**, 93-100, doi:10.1083/jcb.201605097 (2017).
44 Yano, S. *et al.* Invading cancer cells are predominantly in G0/G1 resulting in chemoresistance demonstrated by real-time FUCCI imaging. *Cell Cycle* **13**, 953-960, doi:10.4161/cc.27818 (2014).
45 Belletti, B. *et al.* Stathmin activity influences sarcoma cell shape, motility, and metastatic potential. *Molecular biology of the cell* **19**, 2003-2013, doi:10.1091/mbc.E07-09-0894 (2008).
46 Zilberman, Y. *et al.* Regulation of microtubule dynamics by inhibition of the tubulin deacetylase HDAC6. *J Cell Sci* **122**, 3531-3541, doi:10.1242/jcs.046813 (2009).
47 Bourgonje, A. M. *et al.* Intracellular and extracellular domains of protein tyrosine phosphatase PTPRZ-B differentially regulate glioma cell growth and motility. *Oncotarget* **5**, 8690-8702 (2014).
48 Yamamoto, N. *et al.* Cellular dynamics visualized in live cells in vitro and in vivo by differential dual-color nuclear-cytoplasmic fluorescent-protein expression. *Cancer Res* **64**, 4251-4256, doi:10.1158/0008-5472.CAN-04-0643 (2004).
49 Sayers, C. M. *et al.* Identification and characterization of a potent activator of p53-independent cellular senescence via a small-molecule screen for modifiers of the integrated stress response. *Molecular pharmacology* **83**, 594-604, doi:10.1124/mol.112.081810 (2013).
50 Keys J., W. A., Lammerding J. (2018) Assembly and Use of a Microfluidic Device to Study Cell Migration in Confined Environments. In: Gundersen G., Worman H. (eds) The LINC Complex. Methods in Molecular Biology, vol 1840. Humana Press, New York, NY.
51 Elacqua, J. J., McGregor, A. L. & Lammerding, J. Automated analysis of cell migration and nuclear envelope rupture in confined environments. *PLoS One* **13**, e0195664, doi:10.1371/journal.pone.0195664 (2018).
52 Gonzalez, R. C., Woods, R.E., Eddins, S.L. Digital Image Processing Using MATLAB. *Gatesmark Publishing* **2nd ed.** (2009).

53 Nishitani, H., Taraviras, S., Lygerou, Z. & Nishimoto, T. The human licensing factor for DNA replication Cdt1 accumulates in G1 and is destabilized after initiation of S-phase. *J Biol Chem* **276**, 44905-44911, doi:10.1074/jbc.M105406200 (2001).

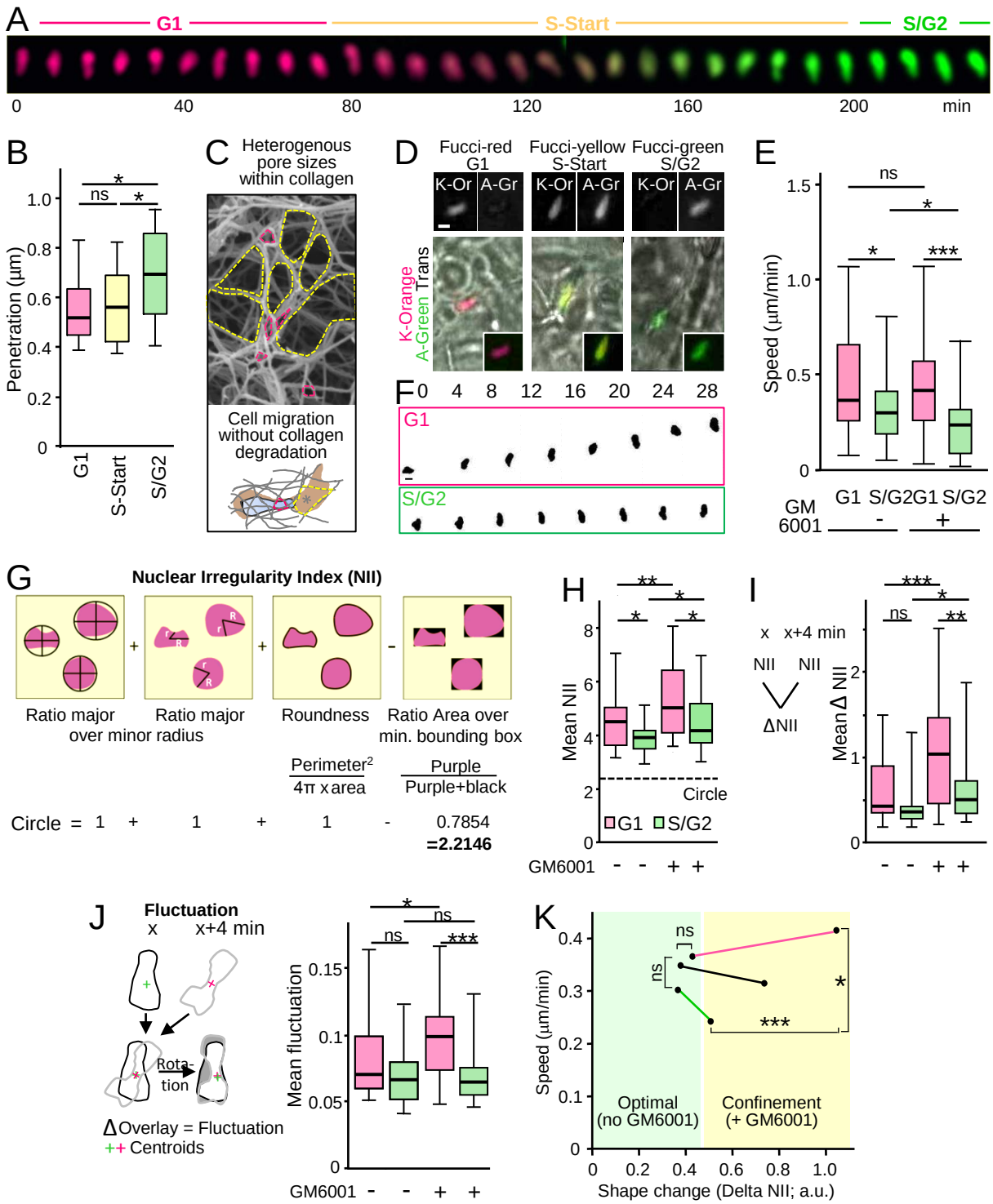

Figure 1. Maintenance of migration through confining pores is associated with shape change of the small and rigid G1 cell cycle phase nucleus. (**A**) Sequence of a cell nucleus from a Fucci-positve HT1080 cell progressing through the cell cycle, as indicated by changing color coding over 4 hours. This sequence is part of Fig. S2 and Movie S1. **(B)** Quantification of cell deformation ('penetration') after 2 nN contact force by a bead-coupled cantilever connected to an atomic force microscope (quantified from the approach curve; Fig. S1D). N = 3; 25-32 cells per indicated cell cycle phase. **(C)** Top, example of collagen matrix (monitored by scanning electron microscopy as shown in [4]) showing small pore areas (confining; marked in pink), adjacent to large pores (marked in yellow). Bottom, cartoon depicting cell and nucleus in collagen of heterogenous, color-coded pore areas, including open space for translocation of cell and nucleus (asterisk). **(D-F)** HT1080- Fucci cells migrated in collagen (1.7 mg/ml) in the presence of MMP inhibitor GM6001 (except where absence of GM6001 is indicated), as monitored by pathway microscopy. (**D**) Examples of migrating cells at different indicated cell cycle phases. (**E**) Averaged migration speed of single cells from Fucci-red or -green populations from movies of 5-24 h length at indicated conditions. Because the S-start phase covers a short, around 2 hour, time period, from here on and in all further experiments G1 phase cells were compared with S/G2 cells only. N = 2-3; 40-65 cells per condition. **(F)** Nuclear segmentation of migrating HT1080-Fucci cells. Time in minutes as indicated. **(G-J)** Nuclear shape analysis. **(G)** Top, schematic illustration of the components used for the calculation of the nuclear irregularity index (NII). Adapted from [36]. Bottom, calculation of all components that describe a circle, resulting in a NII of 2.2146. (**H**) Mean NII values per cell were computed and calculated from each nuclear shape sequence over time. (**I**) Left, scheme for calculation of the difference between subsequent NII's as delta NII, where rapid shape change of the nucleus results in a high delta NII value. Right, mean values of delta NII from each nuclear shape sequence over time. (**J**) Nuclear fluctuation analysis, sketching the analysis procedure (left), and mean values of the fluctuations from each nuclear sequence to the next (right). In **(H-J)**, mean value per cell over 36-316 minutes; n = 3; 38 and 29 cells per G1 and S/G2 phase, respectively. **(K)** Summary of speed as a function of nuclear shape change (delta NII) in optimal and confining collagen conditions (data are from **(E,I)**. Dots connected by red line represent G1 cycle cells; by green line, S/G2 cycle cells; by black line, G1 and S/G2 cycle cells together. **(B,E,H,I,J)** Black horizontal lines, boxes and whiskers show the medians, 25th/75th, and 5th/95th percentile (**B,** 10th/90th percentile), and ***, P ≤ 0.001; **, P ≤ 0.01; *, P ≤ 0.05; ns, non-significant (Mann Whitney test). All image bars, 10 µm.

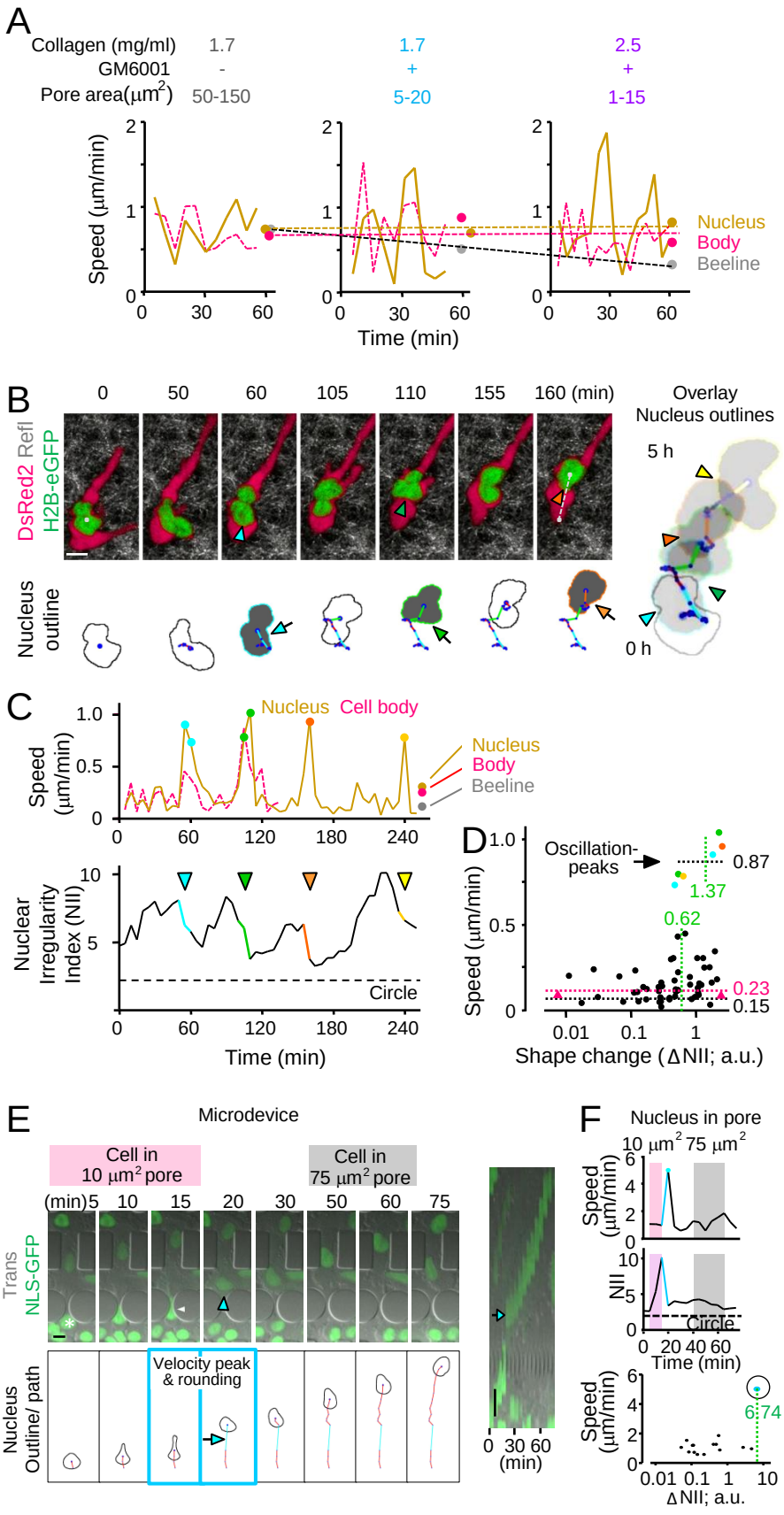

Figure 2. Speed oscillation and rapid nuclear rounding during cell migration in confining pores. HT1080 fibrosarcoma cells moved either in collagen **(A-D)** or in a synthetic microdevice **(E,F)**. **(A)** Cells migrated in collagen of increasing density and the absence or presence of GM6001 as indicated, resulting in depicted decreasing effective pore areas (top; [35]). From each 3 cells, speed of nucleus and cell body was quantified from the migration tracks from the center of the nucleus as well as the cell body that often demonstrated synchronous speed peaks. In addition, the overall migration speed was measured as 'beeline' between the center of nuclei from the first and last image as depicted in Fig. S4 and normalized over 55 min. **(B-D)** Oscillatory speed peaks of the cell and nucleus during migration coincide with nuclear rounding. **(B)** Upper row, left, sequences of HT1080 dual-color cell moving within high density bovine collagen (3.3 mg/ml) monitored by confocal microscopy at 37°C at 5 min intervals [13]. White dots at first and last image and dotted white line indicate position and beeline of the migrated nucleus. Lower row, left, outlines of the nucleus generated from H2B-eGFP signal, with centroids (blue dots) and centroid-connecting movement trajectories in red. Long trajectories indicated in cyan, green and orange and by arrows represent peak movements, and respective nuclear roundings are marked by colored outline and grey area in the outline. Right, overlay of the first and all rounded outlines, and trajectory of the nucleus over 5 hours (corresponding to Movie S4). **(C)** Upper graph, step-to-step and average speed quantification from the movement trajectories of moving cell body and nucleus from (B), as well as the beeline of the migrated nucleus. Repeated speed peaks ('oscillations') of the nucleus are indicated by respective colored dots. Lower graph, corresponding repeated phases of nuclear rounding measured as NII, indicated by respective colors and arrowheads. **(D)** Speed as a function of delta NII per time step (=dot) of the moving nucleus shown in (B), and quantified in (C). Top right, note the link between high speed of forward movement (peak oscillations) and rapid rounding of the nucleus, shown by dots in colors respective to (B,C). All numbers and dotted lines in black and green indicate medians of speed and delta NII, respectively, for either colored oscillation peaks or all remaining dots. Dotted line and number in pink indicate speed median from all dots. **(E)** Migration in microdevice of 10 and 75 mm² pore areas (corresponding to Movie S5, 2. part). Left, upper row, sequence of migrating cell over indicated time. White arrowhead, deformed nucleus in pore. Arrowhead in cyan indicates rounding. Lower row, nuclear outlines with centroids as blue dots and trajectories in red. Arrow indicates long trajectory in cyan that corresponds to nucleus rounding. Right, kymogram, visualizing rapid forward movement (arrow) after transmigration of narrow pore. **(F)** Speed and corresponding NII, with color coding matching imaging sequence. Bottom, speed - nuclear shape change relationship; number in green, delta NII value for peak oscillation. Reprinted modified images in (B) are with permission from Elsevier [13]. All image bars, 10 μm.

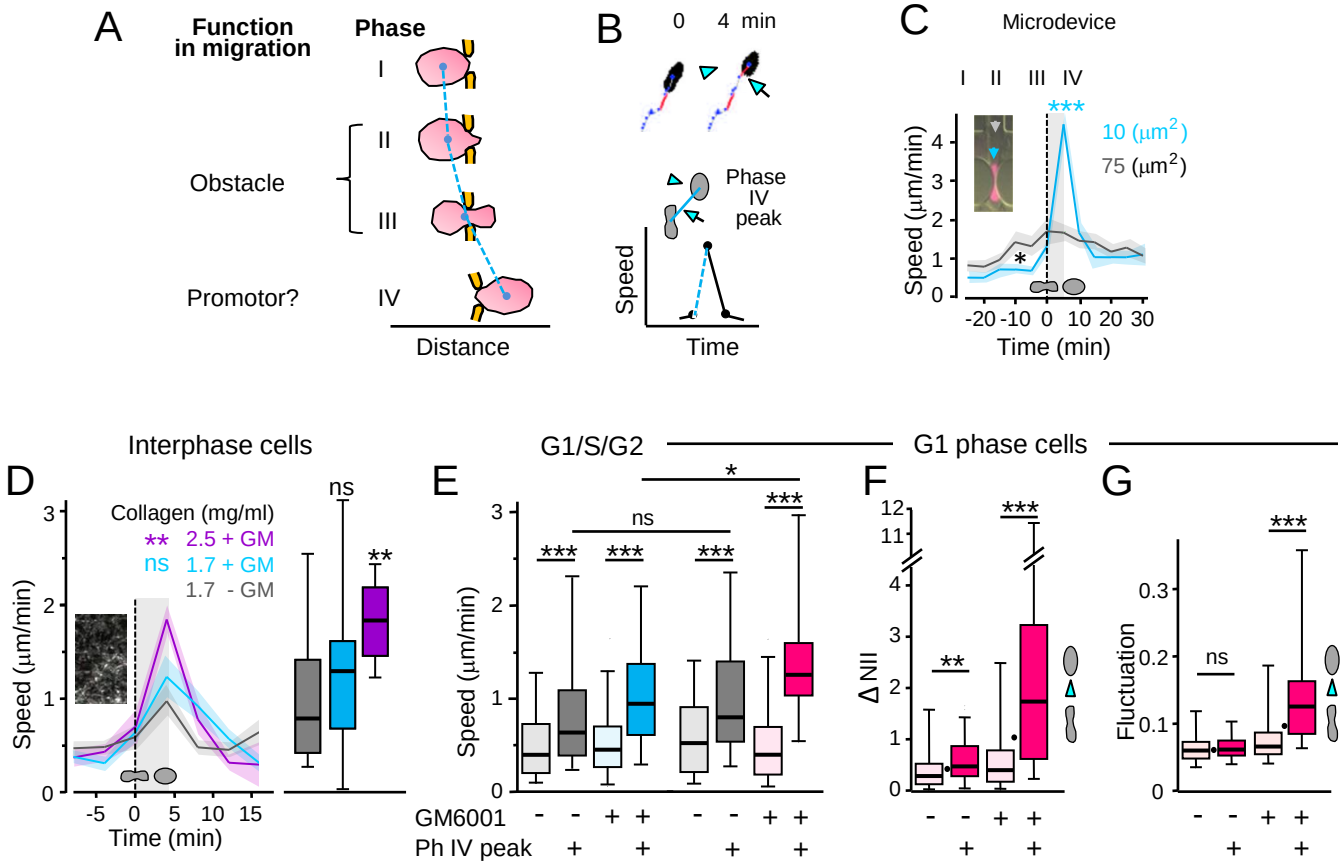

Figure 3. Characterization of 'phase IV' peak events. **(A)** Concept of nuclear deformation phases during cell migration through narrow pores. Adapted from [13]. **(B)** Cartoon depicting selection scheme for phase IV speed peak values connected to nuclear rounding as shown in **(C)** and **(D)**. **(C)** Speed of nuclei before (phase I and II), during (phase III) and after (phase IV) transmigration of pores of 75 mm^2 (grey) and 10 mm^2 (cyan) cross-section from microdevice. Vertical dotted line indicates time point when nuclei passed the center of the pore (see inset), and grey shadowed area indicates phase IV. Solid lines represent mean, and shadowed colored area +/- SEM. 21 cells per condition, n=3. P value was calculated for speed peaks at 5 min after pore passage of 10 mm^2 as compared to data from 75 mm^2 pores. Asterisk indicates decreased speed during passage of small as compared to big pores. **(D)** Quantification of phase IV-speed peaks in collagen of decreasing effective pore size. The onset of each speed peak event was normalized to 0 min (dotted vertical line) and calculated based on speed increase in the moment of nuclear rounding (see black boxes in Fig. S4,A-C, middle panels; S5A,B). N = 1-3; graphs are superimposed from 8-25 respective events from each 5-8 cells per condition monitored at high resolution; mean (colored solid lines) +- SEM (shadowed colored areas). Grey shadowed area indicates phase IV event. Values of the peak speeds are also displayed as box plots. P value was calculated for speed peaks at 4 min after pore passage, as compared to data from 1.7 mg/mL collagen in the absence of GM6001. **(E-G)** Depiction and analysis of either phase IV (strong colors) or all remaining non-phase IV events (light colors) from G1 cell cycle phase cells (pink and grey), or mixed G1/S/G2 cell cycle cells (blue and grey; **E, left**) after migration in collagen **(**1.7 mg/mL) and GM6001 where indicated. Analysis of **(E)** speed, **(F)** delta NII as shown in Fig. 1I, and **(G)** nuclear fluctuation, as shown in Fig. 1J, with the difference that instead of a mean value per cell over time, values from each time point of a moving cell were defined and separated into phase IV peak and remaining events selected as in (B). The single dots in (**F,G**) depict the medians from the G1 phase cell results from Figs. **1I,J**. (**E**, left; G1/S/G2 cells) N=1-3; 50-79 phase IV peak events and 363-387 remaining events were analyzed from nuclear sequences of 16-21 cells per condition. **(E,** right **– G**; G1 cells**)** N=1-3; 24-67 phase IV peak events and 180-424 remaining events were analyzed from nuclear sequences of 8-13 cells per condition. In **(D-G)**, data are depicted as horizontal lines, boxes and whiskers for medians, $25^{th}/75^{th}$, and $5^{th}/95^{th}$ percentile. For all experiments, ***, P ≤ 0.001; **, P, <0.01; ns, non-significant (both Mann Whitney and Kolmogorow test).

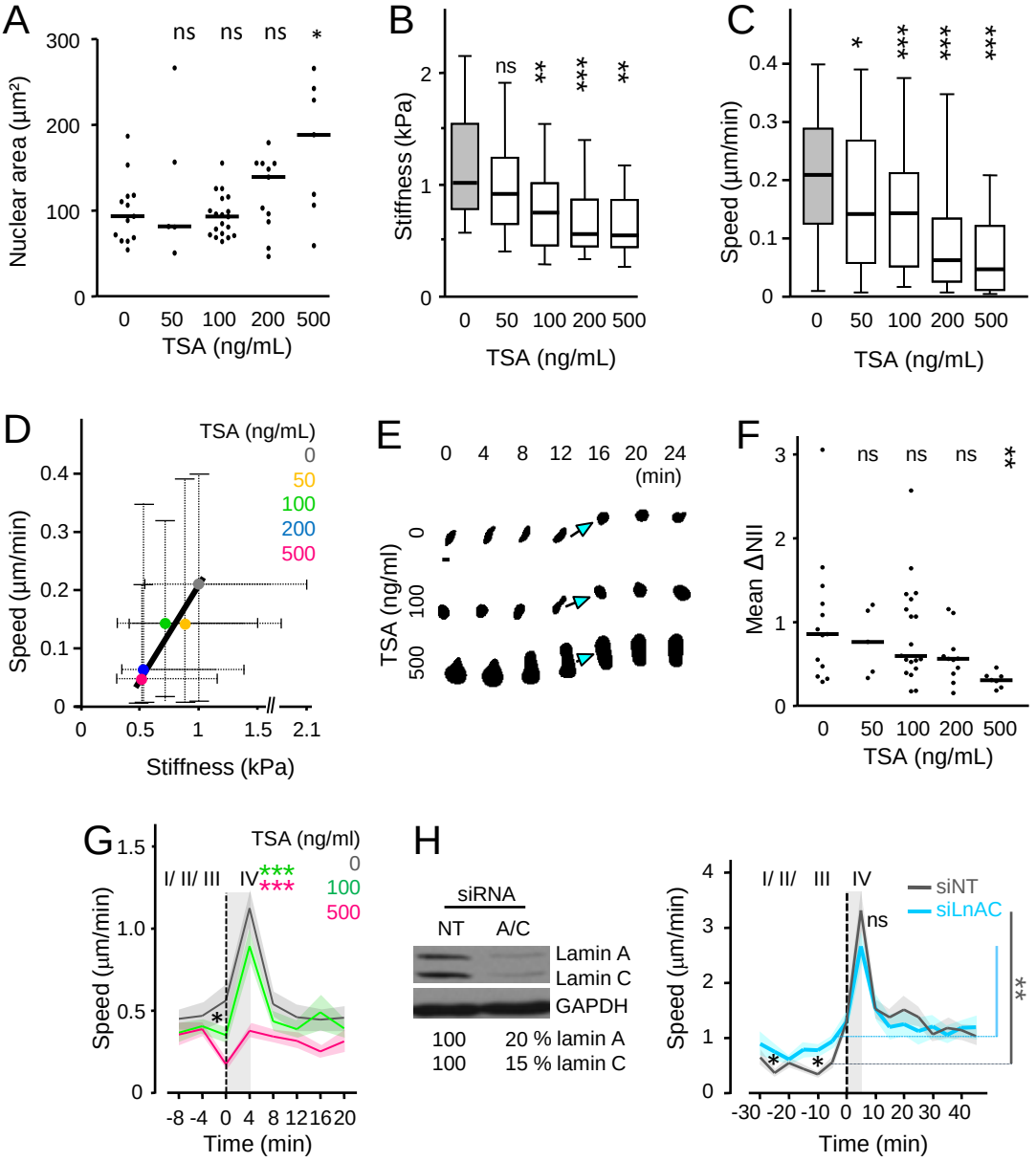

Figure 4. Altered stiffness, migration and reshaping of HT1080 cells and nuclei after TSA treatment or lamin A/C downregulation. Cells were pre-treated with indicated TSA concentrations or DMSO alone (indicated as 0 ng/mL TSA), and were either measured for elastic modulus **(B)** or migrated in collagen (1.7mg/ml) in the presence of GM6001**(A,C-F)**. For all TSA experiments, except in **(B)** and **(C)**, Fucci cells were used and G1 phase cells only were selected for analysis. **(A)** Nuclear areas after pre-treatment with TSA in collagen. Horizontal black lines show the medians. N=1; 5-19 cells per TSA concentration. **(B)** Calculated stiffness at 1.5 nN contact force by bead-coupled cantilever probing using atomic force microscopy. 14-37 cells per condition; n = 1-3. **(C)** Mean cell migration efficacy per cell over 24 h with increasing concentrations of TSA as compared to DMSO control. Cells that underwent mitosis during the recording were excluded from the analysis. N = 3; 66-90 cells per condition. **(B,C)** Horizontal black lines, boxes and whiskers show the medians, 25th/75th, and 10th and 90th **(B)** and 5th/95th **(C)** percentile. **(D)** Correlation of stiffness with migration efficacy, using the medians and whiskers from (A,B). R^2 = 0,92. **(E)** Representative segmented nuclear sequences from migrating G1 phase (Fucci-red) cells at indicated time steps, in correspondence to Movie S6. Arrows indicate phase IV peak events based on speed increase and concomitant nucleus rounding. Bar, 10 mm. **(F)** Nuclear shape change during migration by TSA. Mean delta NII per cell migrating over 0.3 to 10 h. Zero means no changes between subsequent nuclear shapes. 5-19 cells per condition, shown as dots. Horizontal black lines show the medians. **(G)** Speed peaks, as in Fig. 3C, at indicated TSA concentrations. Graphs are superimposed from 22-38 respective events from each 7-19 cells per condition; n = 1. Mean (colored solid lines) +- SEM (shadowed colored areas). Asterisk indicates decreased nuclear speed after TSA treatment before phase IV peak. **(H)** Left, lamin A/C expression intensity by western blot after transient downregulation by indicated siRNA (each 10 nM). Right, speed peaks in cells treated with non-targeting and LaminA/C siRNA after transmigration of 10 µm^2 pore. Asterisks indicate increased nuclear pore negotion speed after silamin A/C treatment before phase IV peak event. Each 21 cells per condition. **(G; H, right)** Dotted vertical lines, speed peak at nuclear rounding; grey-shadowed areas, phase IV events. ***, P ≤ 0.001; **, P ≤ 0.01; *, P ≤ 0.05; non-significant. n.s.; (**A,B,C,F,** Mann-Whitney test; **G, H** Students t-test).

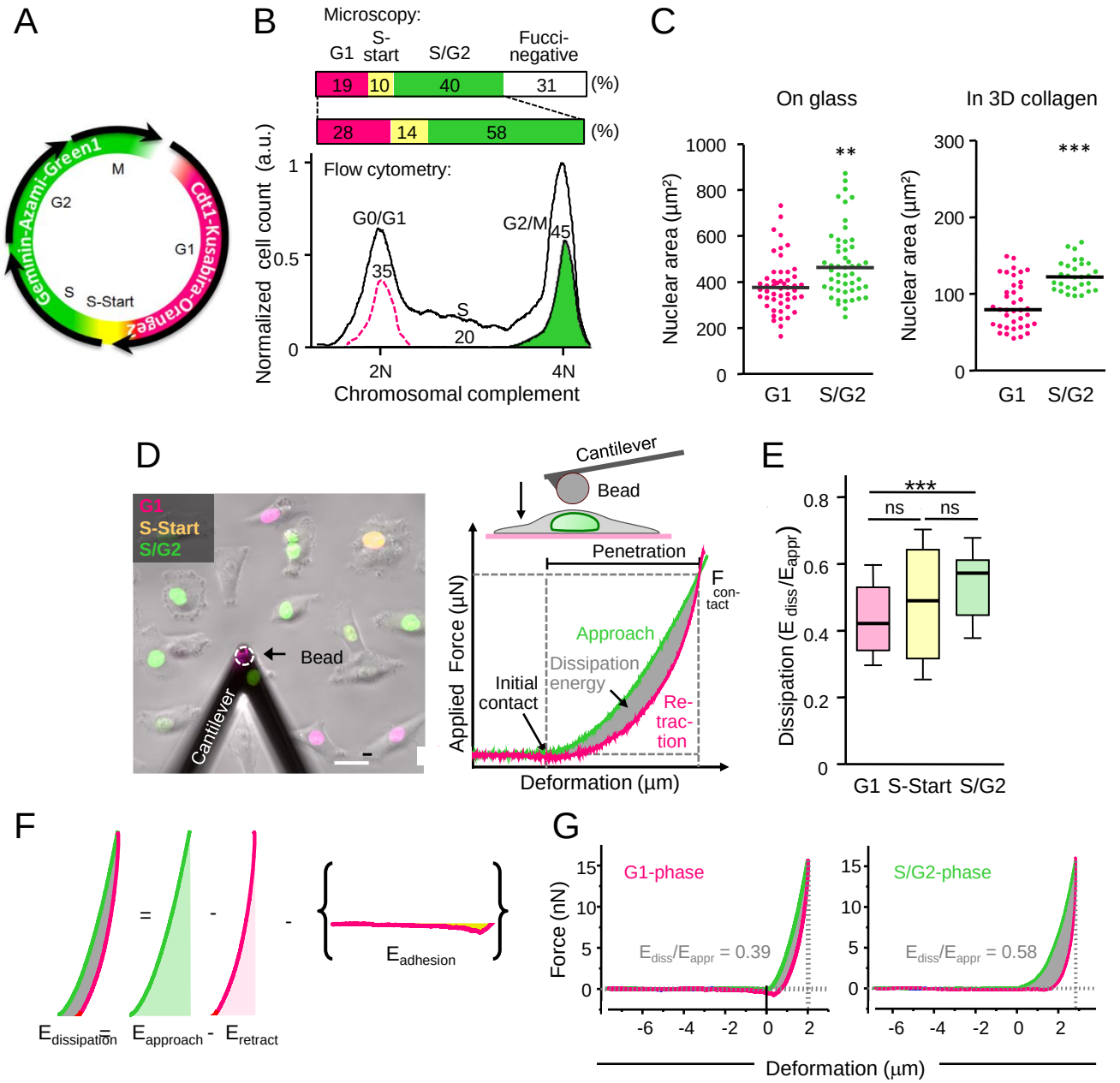

Figure S1. Characterization of HT1080 cells after stable transduction with Fucci vector.

(A) Cartoon of fluorescence ubiquitination-based cell cycle sensor Fucci, adapted from the ThermoFisher Scientific website, demonstrating how cell cycle stages can be optically separated by color coding. The Fucci biosensor exploits the cell cycle-regulated proteolysis of Cdt1 and Geminin, two proteins involved in licensing of replication origins [53]. Ctd1- Kusabira-Orange2 expression is assigned to G1 phase (Fucci-red), which is degraded by the ubiquitin proteasome system when S phase is commencing. Reciprocally, Geminin-Azami-Green1 expression is assigned to the S, G2, and M phases (Fucci-green) and is rapidly broken down upon exit of mitosis. Consequently, cells express both colors (Fucci-yellow) only during the early S phase. Because before cell experimentation the detached and only loosely attached mitotic cells are washed away, green colored cells are in the following termed S/G2. **(B)** Distribution of cell cycle stages in HT1080 cells. Top, percentage of G1, S, and S/G2 phase distributions from 387 adherent cells from 2D cell culture. Bottom, flow cytometric analysis of an ethanol-fixed cell population. Chromosomal complementation is displayed as diploidic (2N) that refers to cells in G1 phase whereas the tetraploidic (4N) cell population refers to cells in S/G2 phase. Cells in S-start phase are distributed in between 2N and 4N, as chromatin duplication is not yet completed. Numbers within compartments are estimated fractions in percent. Back-gating confirmed that S/G2 Fucci-green cells (small peak in green) fill part of the 4N-related peak meaning that they have completed DNA duplication. Dotted pink line indicates the anticipated Fucci-red cell population, as Cdt1-Kusabira-Orange2 fluorescence was lost during fixation. **(C)** Nuclear areas in G1 and S/G2 phase, measured from cells either plated on glass or in collagen. Median, horizontal line. N=2, 51 cells per cell cycle phase (on glass); n=3; 38 and 29 cells per cell cycle phase (in collagen). **(D)** Principle of AFS-force measurements (see [31]). Image and cartoon show that prior to a measurement, a 10 µm-diameter-sized bead immobilized on an cantilever was positioned above the center of the nucleus. Cells were selected by epifluorescence microscopy mode for suitability by morphology and cell cycle phase. After cantilever-mediated approach, compression, and retraction from the cell, the resulting force-distance curves were plotted (graph). Image bar, 20 µm. **(E)** Relative dissipation energy, derived as the area between approach (E_{appr}) and retraction (E_{diss}), and divided by the energy needed to deform the nucleus (E_{appr}). A value of 0 represents a purely elastic nucleus where approach and retraction curves overlap (the nucleus recoils completely, and all of the compression energy is recovered); increasing values indicate increasingly viscous material behavior, including plastic deformation and viscous dissipation of the energy required to compress the nucleus (the nucleus remains partially deformed after the cantilever has been retracted). N = 3; 30-32 cells per condition. Black horizontal lines, boxes and whiskers show the medians, 25th/75th, and 10th/90th percentile. **(F)** Cartoon depicting how the disspation energy was extracted from force-distance curves after a compression-relaxation cycle of a cell when probed by a bead-functionalized cantilever. **(G)** Two example curves of each nucleus in G1-phase and in S/G2-phase show the differences in dissipation indicative for the significant difference found in **(E)**. ***, P < 0.001; **, P < 0.01; ns, non-significant (Mann-Whitney test).

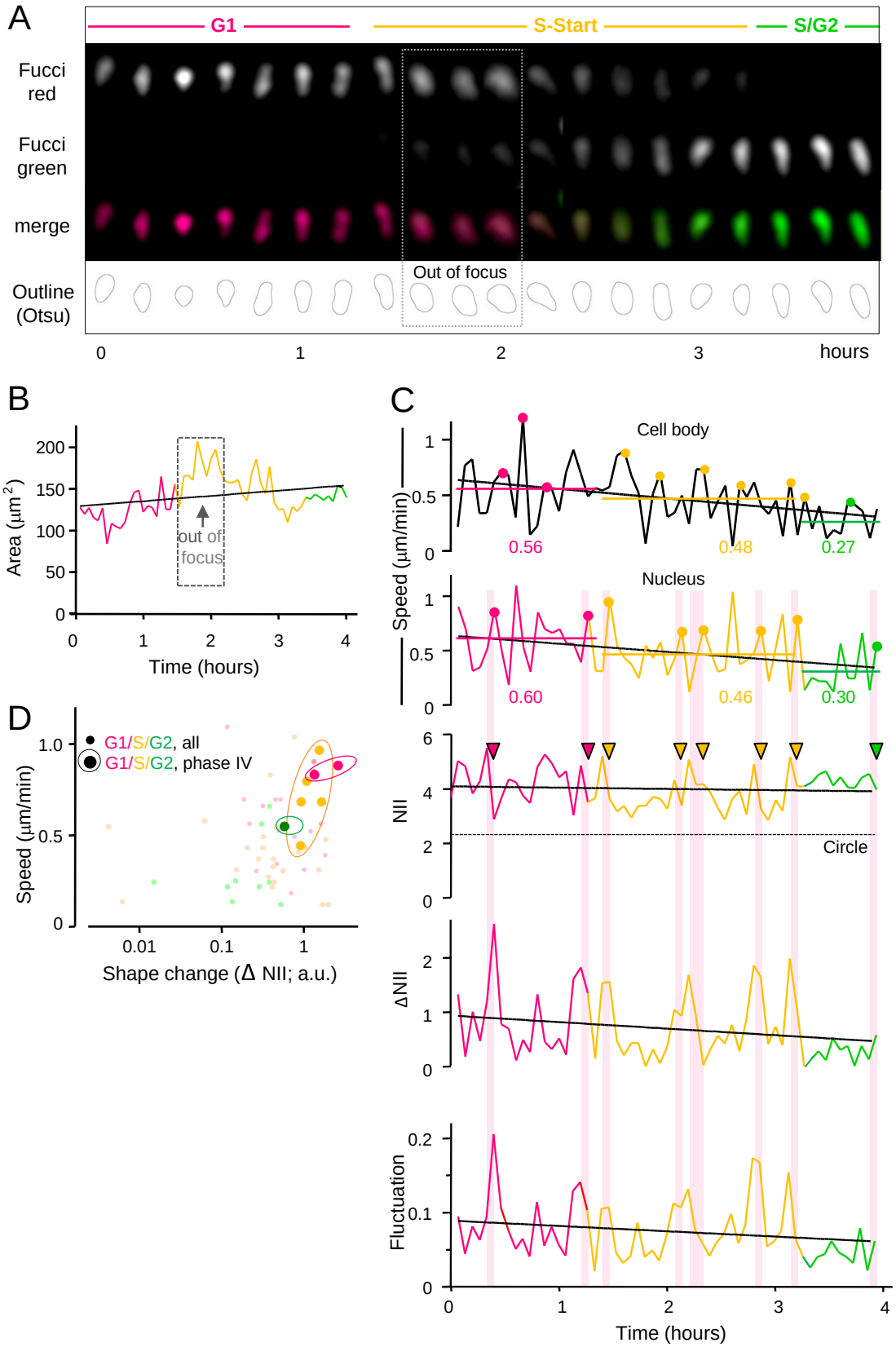

Figure S2. Analysis of cell cycle transition-related nuclear parameters by imaging of a single HT1080-Fucci cell. **(A)** Image sequence from a single migrating cell in collagen in the presence of GM6001, demonstrating a single cell cycle transition over 4 hours (see Fig. 1A and Movie S1). Upper lanes, single red, single green and merged channels. Lowest lane, nuclear outline produced in Fiji ImageJ by Otsu-thresholding. (**B,C)** Quantification of indicated parameters showing each of the gradual change over 4 hours. The up- or downwards trend is indicated by black lines obtained by the trendline function in Fiji, and this trend as well as all quantifications coincide with population data in Figs. 1 and S1. Pink, yellow and green colors indicate the different cell cycle phases as marked in A. **(B)** Quantification of increasing nuclear area during G1 to S/G2 phase transition. Grey shadowed area, out of focus region as marked in (A). **(C)** Top graph, speed fluctuation of cell body. All other graphs, from second top to bottom, quantification of speed and morphometric parameters (NII, delta NII, and fluctuation) of the nucleus, all decreasing from G1 to S/G2 phase. Speed- nuclear shape change relationship for identification of phase IV events are marked by vertical pink lines, and are shown as colored path segments in Movie S1. **(D)** Depiction of phase IV events (encircled) versus all events, color-coded per cell cycle phase. Quantification coincides with population data in Figs. 2D and S5C.

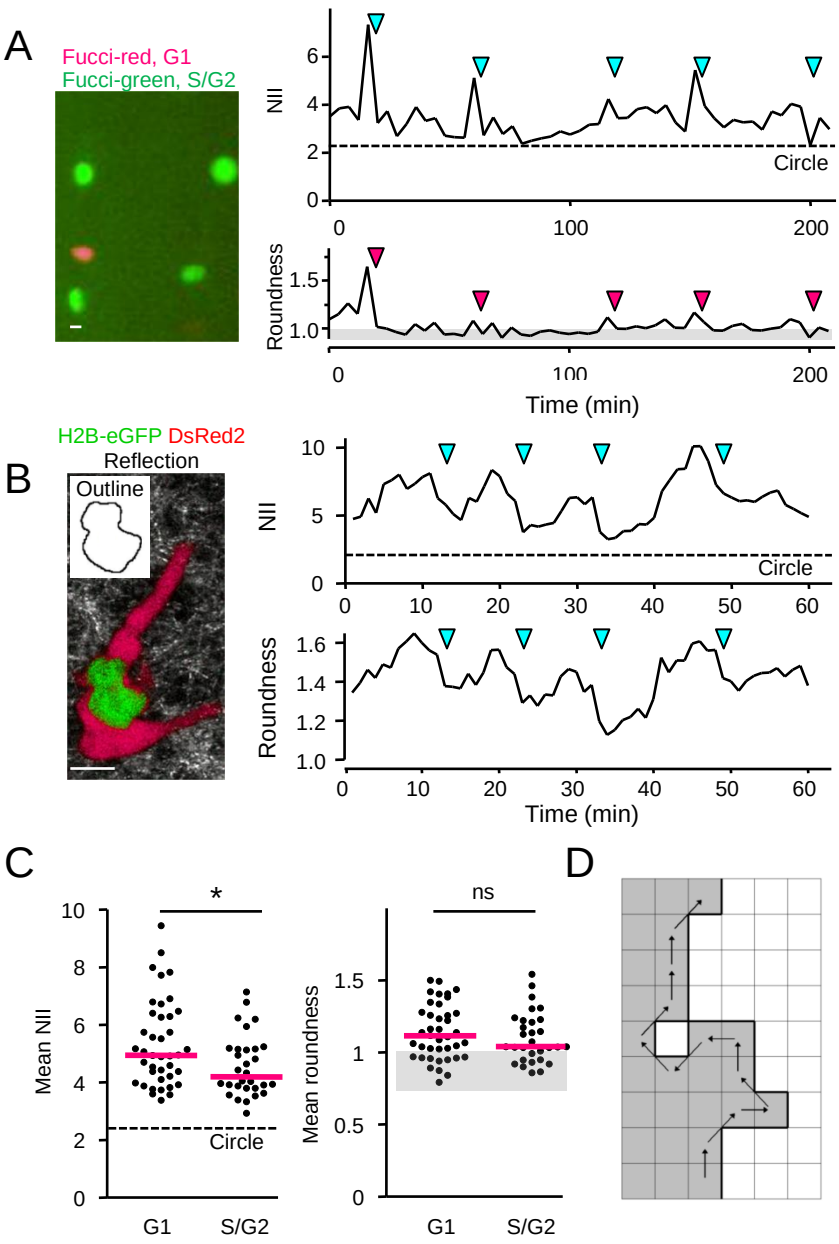

Figure S3. Depiction of the advantage of nuclear irregularity index versus nuclear rounding calculation. **(A)** Left, depiction of nuclei from 5 cells carrying the Fucci construct. Right, graphs show calculation of nuclear shape change for a nucleus from a migrating cell over time, using NII (formula introduced in Fig. 1G) and roundness. Colored arrowheads indicate nucleus rounding. Top, value for a circle is indicated; bottom, area in light grey indicating around 50% roundness values that oscillate around 1 [see explanation in **(D)**]. Thus, when a relatively low-resolution image is used, a single shape property like roundness can be unreliable, but NII with a combination of four shape properties is still robust, indicating the expected shape changes more clearly. **(B)** Left, depiction of nucleus from high-resolution imaging (Fig. 2B); right graphs, depicting NII and roundness and indicating convincing agreement. **(C)** Mean nuclear shapes calculated from single G1 and S/G2 phase cells monitored at low resolution. Difference is significant after calculation of NII, but not after calculation of roundness. Area in light grey indicates roundness values oscillating around 1. Because of roundness' unreliability in low resolution imaging, NII was chosen over roundness. **(D)** Schematic illustration of how the nucleus perimeter was calculated within the calculation of roundness. Rather than a simple edge count method, a polygonal approximation was implemented. This approximation took into account the inward and outward corners, and straight lines. Different weights were assigned, since a digital representation of a shape can only be pixelated without smooth curves. Such an approximation with enough pixels improves the calculation of the perimeter, whereas less pixels entail an under-estimation of the perimeter with a value below 1. All image bars, 10 μm.

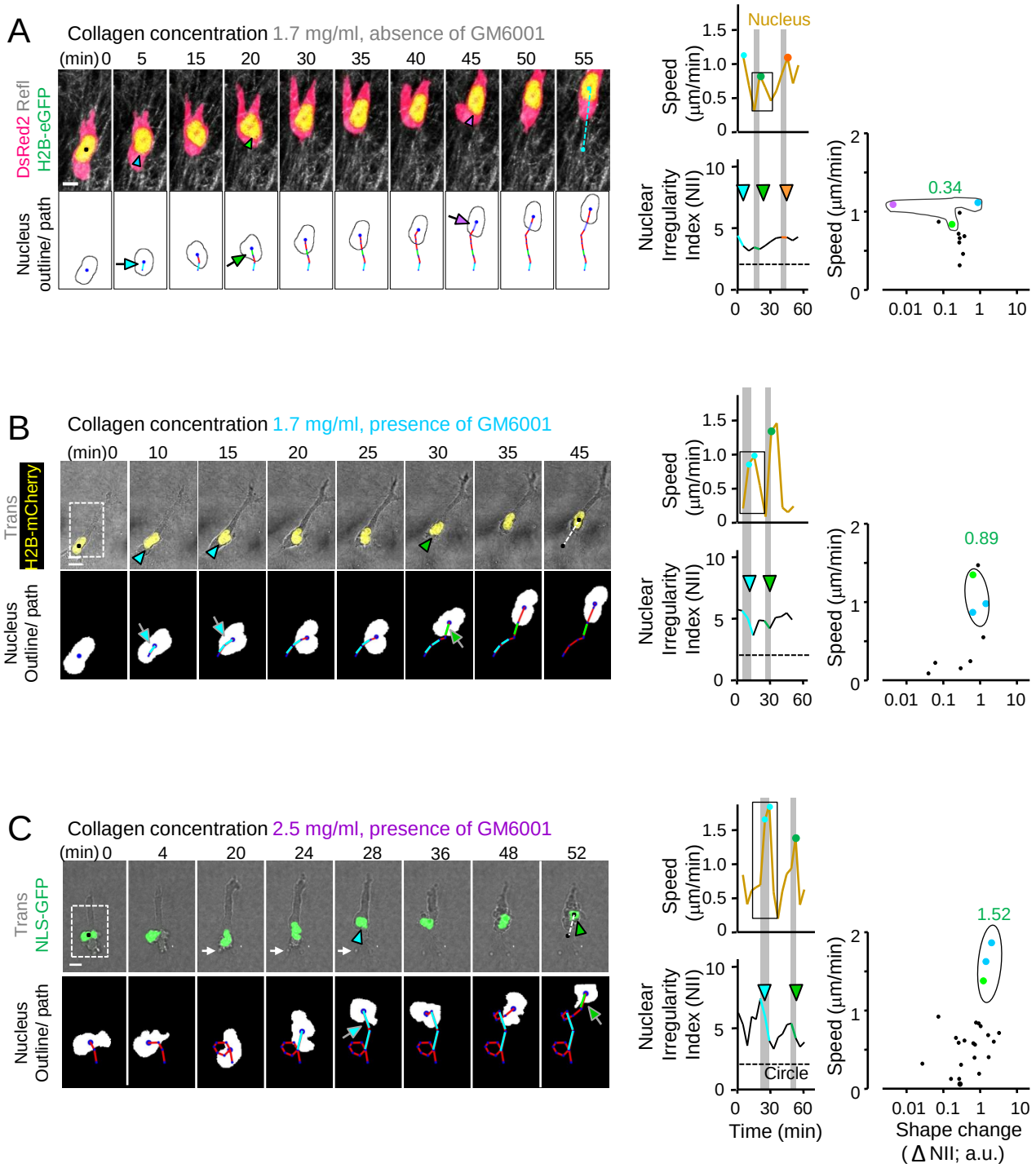

Figure S4. Speed peaks and rounding of the nucleus increase with confinement. HT1080 cells migrated in collagen of increasing indicated concentrations and the absence or presence of GM6001 (sequences and values correspond to Fig. 2A). **(A-C) Left column,** upper rows, sequences of migrating cells over indicated time periods and in indicated colors for cell body (DsRed2 or transmission signal), nucleus (H2B-eGFP, H2B-mCherry or NLS-GFP) and collagen reflection signal. Color-coded arrowheads indicate rounding even if marginal. Lower rows, nuclear outlines or segmentations, respectively, with centroids as blue dots and trajectories in red. Arrows indicate long, colored trajectories that correspond to nucleus rounding indicating phase IV peak events. **(B,C)** Dotted rectangle, inset where nucleus in bottom row was enlarged from. **(C)** White arrows, detachment of cell rear corresponding to velocity peak and rounding of nucleus. All bars, 10 mm. **Middle column,** speed patterns of nuclei (top), and corresponding NII value, all with color coding matching events in imaging sequences. Speed peaks that associate with decreasing NII values ('phase IV peak events') are indicated by colored dots and grey areas, and representative speed peak sizes are indicated by length of black boxes. **Right column**, speed as a function of delta NII, where values that relate to color-coded speed peaks/nuclear rounding are encircled, and numbers in green, median value of respective delta NII. Part of the image sequence from **(C)** is reproduced from [35].

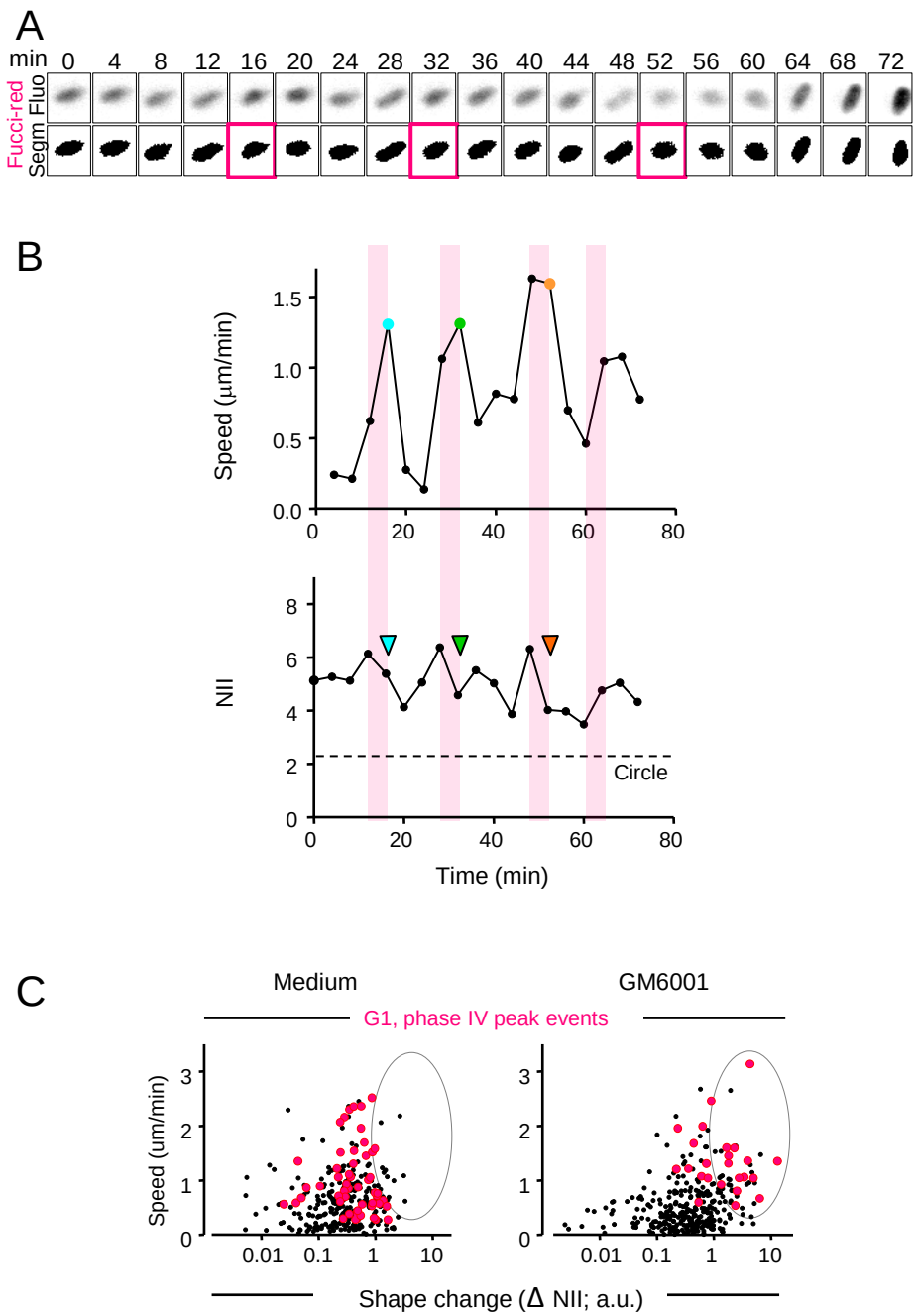

Figure S5. Selection and depiction scheme of phase IV speed peak/ nuclear rounding events. **(A)** Imaging sequence and segmentation from a representative G1 phase HT1080-Fucci cell nucleus migrating in collagen (1.7 mg/ml) in the presence of GM6001. **(B)** Analysis of the nuclear parameters speed and NII, and simultaneous display over time to demonstrate how phase IV nuclear events were selected according to when a speed peak was associated with a decrease of NII from one timestep to the next. Phase IV events are marked by colored dots and vertical pastel-colored stripes, and the corresponding rounded nuclear shapes in **(A)** are marked by red-colored outline. **(C)** Phase IV (pink dots) and non-phase IV (black dots) events from G1 phase cell nuclei from cells migrating in collagen (1.7 mg/mL) and in the absence and presence of GM6001, where speed is shown as a function of delta NII values per time step (data points and cell numbers correspond to Fig. 3E right;F). Colored ellipses indicate increased shape change of phase IV events in right graph as compared to left graph.

Overview supplementary movies

Movie S1

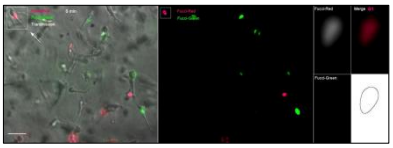

Movie S1. Spontaneous migration of mesenchymal HT1080-Fucci cells over different interphase cell cycle phases. Migrating HT1080-Fucci cells in 3D collagen in the presence of GM6001 were imaged by pathway microscopy at 37°C. Fluorescently labeled nuclei (**middle panel**) were overlaid with brightfield signal showing polarized cell bodies within 3D collagen in different layers (**left panel**). Marked cell in left-upper corner migrated to the right-lower corner while it transited from G1 (pink) to S-Start (yellow) and S/G2 (green) cell cycle phase. In cell track, segments of phase IV peak step-to-step distances, when appearing with nuclear rounding (see colored dots and arrowheads Fig. S2C), were marked in respective Fucci color. **Right panel,** respective crops from the nucleus of the marked cell during cell cycle transition, with forward moving tip of nucleus being directed towards the bottom, together with Otsu-segmented outline, complementary to Fig. 1A and S2A, and used for quantifications in Fig. S2B-D. Time as indicated. Bar, 50 μm.

Movie S2

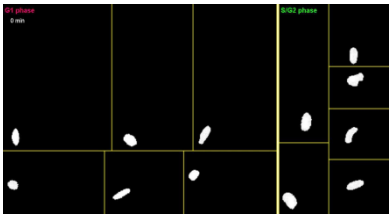

Movie S2. Phase IV peak events in migratory G1 phase HT1080 cells. Segmentation of in focus-HT1080 cell nuclei from G1 (as well as S/G2) phase during cell migration in collagen in the presence of GM6001, cropped from overview image sequences such as Movie S1. In the first part of the movie only the nuclear morphologies are shown, whereas in the second part centroids per segmented nucleus are shown in blue, together with centroid-connecting cell tracks where 'phase IV events' are marked by pink (or green) track segments. G1 phase nucleus sequence marked with asterisk is displayed in Fig. S5A. Time as indicated.

Movie S3

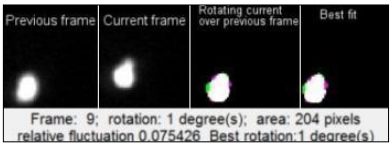

Movie S3. Illustration of the nuclear shape rotation method for fluctuation analysis. The two left columns show the previous and current frames of a sequence separated by 4 minutes each. The second column to the right shows the anticlockwise rotation in 1 degree steps of the 'current' over the 'previous' segmented frame. Non-overlapping areas are shown in pink and green. The right column reflects the 'best fit' with maximum overlap of the 2 shapes, where 0 means complete overlap. Note that the 'best fit' is updated whenever a new maximum overlap is found during the rotation. This analysis tool corresponds to fluctuation analysis used in Fig. 1J.

Movie S4

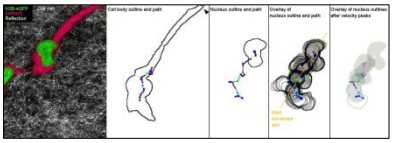

Movie S4. HT1080 dual-color cell in dense collagen: oscillatory migration and repeated rapid rounding of the nucleus. Cell migrates within bovine collagen (3.3 mg/ml; reflection signal) by shape change of cell body (DsRed2) and nucleus (H2B-eGFP), as imaged by confocal microscopy at 37°C over 5 hours (left). Each computed outline of cell body and nucleus contains a centroid (blue) that progressively forms migration paths (pink). Long path segments marked in cyan, green, orange and yellow color in both cell body and nucleus associate with rapid nuclear rounding (grey filling) and represent 'phase IV peak events'. Progressing outline of cell body stalls at 135 min as pseudopod leaves image field (black arrowhead). Nucleus outlines presented either as simple progressing (middle), progressive overlay of outlines (second to the right) and as overlay of grey rounded areas after oscillatory velocity peaks. Movie corresponds to Fig. 2B. Time as indicated. Bar, 10 μm.

Movie S5

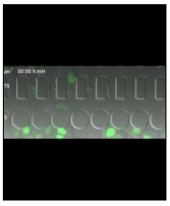

Movie S5. Migration of HT1080 cells through synthetic microdevice. Cells transfected with NLS-GFP migrated through indicated 10 mm^2 and 75 mm^2 pores of a microdevice over 9 h (first movie part) or around 1 h (second movie part). Green, NLS-GFP signal; transmission, PDMS pillars and cell bodies. Arrowheads indicate examples of nuclear passage through pore center, of which events were used for Fig. 3C (first movie part) or Fig. 2E (second movie part, with long phase IV-associated trajectory in cyan).

Movie S6

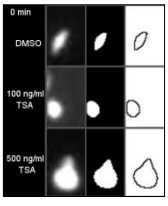

Movie S6. TSA reduces cell migration efficacy and nuclear shape change. HT1080 G1 phase (Fucci-red) cells, after pre-treatment by DMSO or TSA moved in collagen in the presence of GM6001. Note the size increase of the nucleus after pre-treatment by 500 ng/mL TSA. Comparison of the original fluorescent nuclear shapes (left column) with thresholded segmented counterparts (middle) and outlines (right) illustrate segmentation quality used for this study. Complementary with Fig. 4E. Time as indicated.